University of Alberta

Numerical Modelling of Internal Waves in the Boussinesq and Anelastic Approximations

by

Joshua T. Nault

A thesis submitted to the Faculty of Graduate Studies and Research in partial fulfillment of the requirements for the degree of **Master of Science**.

in

Applied Mathematics

Department of Mathematical and Statistical Sciences

Edmonton, Alberta
Fall 2007

Library and Archives Canada

Published Heritage Branch

395 Wellington Street
Ottawa ON K1A 0N4
Canada

Bibliothèque et Archives Canada

Direction du Patrimoine de l'édition

395, rue Wellington
Ottawa ON K1A 0N4
Canada

Your file Votre référence
ISBN: 978-0-494-33315-0
Our file Notre référence
ISBN: 978-0-494-33315-0

NOTICE:
The author has granted a non-exclusive license allowing Library and Archives Canada to reproduce, publish, archive, preserve, conserve, communicate to the public by telecommunication or on the Internet, loan, distribute and sell theses worldwide, for commercial or non-commercial purposes, in microform, paper, electronic and/or any other formats.

The author retains copyright ownership and moral rights in this thesis. Neither the thesis nor substantial extracts from it may be printed or otherwise reproduced without the author's permission.

AVIS:
L'auteur a accordé une licence non exclusive permettant à la Bibliothèque et Archives Canada de reproduire, publier, archiver, sauvegarder, conserver, transmettre au public par télécommunication ou par l'Internet, prêter, distribuer et vendre des thèses partout dans le monde, à des fins commerciales ou autres, sur support microforme, papier, électronique et/ou autres formats.

L'auteur conserve la propriété du droit d'auteur et des droits moraux qui protège cette thèse. Ni la thèse ni des extraits substantiels de celle-ci ne doivent être imprimés ou autrement reproduits sans son autorisation.

In compliance with the Canadian Privacy Act some supporting forms may have been removed from this thesis.

While these forms may be included in the document page count, their removal does not represent any loss of content from the thesis.

Conformément à la loi canadienne sur la protection de la vie privée, quelques formulaires secondaires ont été enlevés de cette thèse.

Bien que ces formulaires aient inclus dans la pagination, il n'y aura aucun contenu manquant.

Canada

Abstract

Numerical methods are developed to model the propagation of small-amplitude two-dimensional internal gravity waves through non-rotating inviscid fluids in the Boussinesq and anelastic approximations. Using these techniques, transmission coefficients for internal waves in fluids with varying stratification and background shear are found. The transmission and reflection of internal waves incident upon a stratified layer in stationary fluid is analyzed, focusing upon the opposing limits of piecewise-linear theory and heuristic applications of WKB theory. Transmission across critical layers is possible when the Richardson number is less than 1/4. Furthermore, internal waves can partially transmit across mixed regions resulting from the evolution of unstable shear layers. Using the anelastic approximation, it is found that decreasing the density scale height reduces the frequency and wavenumber range over which internal waves may propagate. Finally, internal waves generated by flow over Jan Mayen island are modelled; these waves are found to tunnel into the stratosphere.

Acknowledgements

I would like to thank my family for providing the lifelong support that allowed me to reach this point. In particular I would like to thank my mom, who always made sure I had everything I needed to go to school and learn, my dad, who was always there to help me study, and my grandparents.

Research is very much a collaborative effort and I could not have completed this work without the help of my colleagues. Fellow graduate student Geoff Brown frequently provided insight into this work through discussion of his research. My supervisor, Bruce Sutherland, was invaluable in providing an interesting problem and the support to help shape raw results into meaningful research. Bruce is a talented scholar and an exceptional supervisor. His tireless dedication to research is to be admired.

Finally, thank you all of my friends at the University of Alberta for making my time here very enjoyable.

This work has been supported by the Natural Sciences and Engineering Research Council of Canada (NSERC), the Canadian Meteorological and Oceanographic Society (CMOS) and the Alberta Ingenuity Studentship program.

Table of Contents

1 Introduction **1**

1.1 Thesis Overview 7

2 Boussinesq Numerical Methods **9**

2.1 Introduction 9

2.2 Governing Equation 10

2.3 Numerical Tools Overview 13

2.3.1 Numerical Solver 13

2.3.2 Solution Driver 15

2.4 Transmission Quantification 19

3 Boussinesq Simulations **21**

3.1 Introduction 21

3.2 Code Testing 21

3.3 Stationary Fluid Results 22

3.4 Shear Results 25

3.5 Mixed Layer Results 30

4 Anelastic Numerical Methods **34**

4.1 Introduction 34

4.2 Governing Equation 35

4.3 Numerical Tools Overview 40
4.3.1 Numerical Solver 41
4.3.2 Solution Driver 42

5 Anelastic Simulations **47**
5.1 Introduction 47
5.2 Piecewise-linear Shear 47
5.2.1 Analytic Results 48
5.2.2 Numerical Results 50
5.3 Jan Mayen 56
5.3.1 Background 57
5.3.2 Numerical Results 61

6 Summary and Conclusions **67**

Bibliography **71**

A Frobenius Method **76**
A.1 Introduction 76
A.2 The Taylor-Goldstein Equation 76
A.3 The Anelastic Taylor-Goldstein Equation 78

B Thermodynamic Principles **81**
B.1 Thermodynamic Equations 81
B.2 Numerical Methods 82

List of Figures

2.1 Schematic illustration of wave superposition 18

3.1 Schematic illustration of Boussinesq background profiles . . . 23

3.2 Background profiles and transmission characteristics for buoyancy frequency falloff 24

3.3 Transmission characteristics for shear step profiles 27

3.4 Background profiles and transmission characteristics for evolved shear profiles 31

5.1 Piecewise-linear Boussinesq profiles 49

5.2 Piecewise-linear anelastic profiles 51

5.3 Anelastic transmission characteristics for piecewise-linear shear profiles 53

5.4 Atmospheric buoyancy frequency and horizontal shear measured over Jan Mayen 58

5.5 Reproduction of Figure 9 from Eckermann et al. (2006) – simulated vertical velocity over Jan Mayen 60

5.6 Transmission characteristics for Jan Mayen atmospheric profiles 62

5.7 Calculated streamfunction for mountain generated wave characteristic of flow over Jan Mayen 65

Chapter 1

Introduction

Due to the restoring forces of buoyancy, internal waves propagate through fluids having decreasing background density with height, $\bar{\rho}(z)$. Internal waves vertically transport energy in such stably stratified fluids leading to drag and mixing at levels where they break. Previous studies by Polzin et al. (1997) and Ledwell et al. (2000) have shown that internal waves have a significant effect on ocean mixing. In particular, the 'zonal countercurrents', jets with velocity as large as 25 cm/s observed at depths between 500 m and 3000 m within 2° of the equator (Firing, 1987), are believed to be driven by internal gravity wave breaking. It has been hypothesized that the waves originate at the base of the surface mixed layer (Dillon et al., 1989; Hebert et al., 1991; Skyllingstad and Denbo, 1994) or are generated by shear instability of the upper flank of the equatorial undercurrent (Sutherland, 1996). It is not well understood how the waves propagate through the background shear and stratification particularly when the background variations are manifest on short scales compared with the vertical wavelength of the waves. Shear instability also results in localized mixing in the ocean. Internal waves may still cross a mixed patch in the presence of a critical layer in shear, but the problem has not been well studied.

Similarly, atmospheric internal waves propagate upward through varying

stratification and shear. Internal waves significantly affect the general circulation of the atmosphere (Palmer et al., 1986; McFarlane, 1987). But how they do so depends on how they propagate and where they break. In a particular study near Darwin, Australia internal waves were observed in the ionosphere, where they are visualized by infrared airglow emission from OH molecules, presumably originating from a convective storm beneath (Yamada et al., 2001). Alexander et al. (2004) performed ray tracing studies that linked internal wave observations at higher altitudes to convective sources in the troposphere. These waves propagated through the mesosphere where they became evanescent. Snively and Pasko (2003) proposed that nonlinear wave-wave interactions excited longer-period non-evanescent waves that propagated through the mesosphere and broke in the ionosphere. Walterscheid et al. (2001) performed numerical simulations using observed background stratification to show that without changing their frequency wavepackets were able to penetrate partially through the evanescent region to reach the ionosphere. Generally it is not well understood how internal waves transmit and reflect from the mesosphere when the vertical scale of the waves is comparable to the scale of the background variations.

Eckermann et al. (2006) examined waves generated by wind flowing over the mountain island of Jan Mayen in the North Atlantic. Using Fourier ray tracing models they were able to characterize the internal waves near the surface. However, due to an evanescent region near the tropopause their model breaks down as it does not allow waves to propagate effectively past this region. Fully nonlinear numerical simulations confirm that waves should partially propagate past the tropopause into the stratosphere. They suggest that a mechanism for tunnelling of trapped waves through an evanescent layer is required in

their ray tracing model. Using a Lipps-Hemler model forecast on atmospheric profiles taken on the same day as the Jan Mayen experiment, Eckermann et al. (2006) observed tunnelling of topographically generated internal waves into the stratosphere over northern Scandinavia.

The purpose of this study is to provide a means with which to predict the transmission and reflection of internal waves through arbitrary background states. In the work presented here, we first restrict ourselves to the study of small-amplitude waves in Boussinesq fluid. The Boussinesq approximation is well suited to internal waves in the ocean which propagate over distances much smaller than a density scale height. In later sections the Boussinesq approximation is dropped and anelastic waves considered. In describing these background states for the atmosphere it is necessary to establish a scale over which the background density changes significantly. This is the density scale height, H_ρ, which represents the 'e-folding depth' of exponentially decreasing density with height. Explicitly,

$$H_\rho = \frac{-\bar{\rho}}{\frac{d\bar{\rho}}{dz}} \tag{1.1}$$

where $\bar{\rho}(z)$ is the background vertical density profile. In the atmosphere, typically $H_\rho \sim 8$ km. Atmospheric internal waves may traverse distances much larger than the density scale height, so that the anelastic approximation must be used.

In either the Boussinesq or anelastic approximations, for waves to propagate vertically the Doppler-shifted frequency,

$$\bar{\Omega}(z) \equiv \omega - k\bar{U}(z), \tag{1.2}$$

must be less than the buoyancy frequency, N. Where $\bar{\Omega} > N$ the waves are said to be evanescent. Here ω is the absolute frequency, k is the horizontal

wavenumber and $\bar{U}(z)$ is the background horizontal flow. For a Boussinesq liquid, the squared buoyancy frequency,

$$N^2 = -\frac{\bar{g}}{\rho_{00}}\frac{d\bar{\rho}}{dz}, \tag{1.3}$$

is defined in terms of the gravitational acceleration, g, characteristic liquid density, ρ_{00}, and background density profile, $\bar{\rho}(z)$. The buoyancy frequency is the natural frequency of vertical oscillations in the fluid. For a gas, stratification is conveyed through the potential temperature, $\bar{\theta}(z)$, which is defined as the temperature gas at altitude z would acquire if moved adiabatically to ground level. When considering anelastic internal waves, the squared buoyancy frequency is defined in terms of background potential temperature, $\bar{\theta}(z)$:

$$N_\theta^2 = \frac{g}{\bar{\theta}}\frac{d\bar{\theta}}{dz}. \tag{1.4}$$

For Boussinesq gases, the equivalent squared buoyancy frequency is

$$N^2 = \frac{g}{\theta_{00}}\frac{d\bar{\theta}}{dz}, \tag{1.5}$$

where θ_{00} is the characteristic potential temperature of the gas.

The calculation of energy and momentum transport for propagating internal waves in media with relatively long vertical variations compared with the vertical wavelength is typically performed using 'ray tracing', which applies WKB theory (Lighthill, 1978; Broutman et al., 2004). In the WKB approximation it is assumed that wavefunctions vary rapidly in the vertical with respect to slowly varying background fields $\bar{U}(z)$ and $N(z)$. Heuristic arguments suggest that small amplitude waves will reflect from a level where $\bar{\Omega} = N$ and will asymptotically approach a critical level where $\bar{\Omega} = 0$.

Applying WKB theory, Lindzen and Barker (1985) examined the propagation of internal waves across a critical layer in uniform shear. In their setup

waves were generated in a region of high buoyancy frequency, large enough to allow the wavelike propagation, and then propagated through a region of low buoyancy frequency where the waves encountered a critical layer. Beyond this region the buoyancy frequency again became large. They found that the reflected waves could have larger amplitude than the incident waves, suggesting 'over-reflection'. This study specifically examined waves that resonated with unstable modes and was restricted to hydrostatic waves.

Broutman et al. (2004) discuss several ray tracing techniques and the limitations introduced by caustics, which occur when rays intersect each other, typically near a reflection level. Caustics may be avoided by making a uniform approximation using Airy functions. Other more advanced techniques involve switching between spatial and wavenumber formulations near a caustic to 'step over' the singularity. Although both these techniques can produce valid solutions, they are limited by the WKB approximations.

Resonant energy transfer by internal waves between two localized regions of enhanced stratification representative of the main and seasonal thermocline was described by Eckart (1961). As opposed to theory that invokes the WKB approximation, this study was limited to the examination of modes with vertical wavelength comparable to the characteristic height of the ducts and the separation distance between them. Similarly, resonant energy transfer in the atmosphere between the stratosphere and ionosphere was considered by Fritts and Yuan (1989). This study included anelastic effects and background shear. In both cases the modes periodically transferred energy back and forth between the two ducts.

Our study poses no such restrictions: the vertical wavelength of the incident and transmitted waves is arbitrary and we focus upon the one-way transport

of energy across an arbitrarily specified background stratification and mean flow.

This work extends the results of Sutherland and Yewchuk (2004), who derived formulae that predicted the one-way transport of energy by waves across a weakly stratified layer. They termed this phenomena 'internal wave tunnelling'. In their study they generated waves in a stationary flow with uniform stratification surrounding a finite-depth region of lower or zero buoyancy frequency, a structure they termed an 'N^2-barrier'. Heuristic arguments from WKB theory suggest that waves would completely reflect upon reaching the N^2-barrier. However, this was not the case – significant amounts of wave energy could penetrate the barrier so long as the barrier depth was sufficiently small compared to the horizontal wavelength of the internal waves.

These results were extended further by Brown and Sutherland (2007) who considered the transmission of waves across a critical layer in a piecewise-linear shear flow embedded within a locally unstratified layer. They found that for relatively strong shear it was possible for internal waves to propagate through critical levels.

Eltayeb and McKenzie (1975) also examined the transmission of waves across a critical layer in piecewise-linear shear. However, they introduced a hydrostatic approximation to obtain their analytic solution.

In special circumstances, analytic solutions exist for non-piecewise linear background density and flow profiles. Using hypergeometric functions and neglecting the curvature of the background flow, Duin and Kelder (1981) considered the transmission of waves across a hyperbolic tangent shear layer with constant buoyancy frequency for large Richardson number. Their physical profiles are examined in Section 3.4 of this paper and transmission characteristics

found using the complete linear wave equation for small Richardson number flows.

In the current study, we extend the result of Brown and Sutherland to include transmission across a critical layer where the gradient Richardson number is non-zero. Furthermore, by dropping the Boussinesq approximation, we extend their results to systems where the density scale height is small relative to the length of the domain. As such, anelastic effects are introduced into the system and the significance of density scale height measured. We develop numerical techniques to compute the transmission and reflection of internal waves in arbitrary background buoyancy frequency and velocity profiles in both the Boussinesq and anelastic approximations.

1.1 Thesis Overview

This report is divided into two parts characterized by simplifying assumptions: in Chapters 2 and 3 the Boussinesq approximation is invoked whereas in Chapters 4 and 5 a fully anelastic system is considered.

In Chapter 2, the theoretical background and numerical methods used to compute internal wave propagation, transmission, and reflection in the Boussinesq approximation are discussed. Chapter 3 presents results obtained from the application of the numerical method to several background buoyancy frequency and velocity profiles. Specifically, in Section 3.3 the code is applied to a continuously varying stratification where waves propagate from a strongly stratified to weakly stratified region and we compare the results with predictions of WKB and piecewise-linear theory. In Section 3.4 the effects of a continuously varying background shear in uniformly stratified flow are examined. In Section 3.5 the unstable background flow considered in Section 3.4 is

allowed to evolve nonlinearly to a quasi-steady state consisting of a broader shear profile and locally reduced stratification resulting from mixing and the resulting profiles analyzed.[1]

Chapter 4 presents the theoretical background and numerical methods used to model internal waves in an anelastic fluid. In Chapter 5 the numerical methods are applied to a series of background buoyancy frequency and shear profiles. In Section 5.2 the piecewise linear shear profiles considered by Brown and Sutherland (2007) are examined and the effects of manipulating density scale height analyzed. Section 5.3 examines atmospheric profiles observed over the island of Jan Mayen in the North Atlantic. Mountain generated internal waves are modelled as they propagate upwards through the tropopause into the stratosphere.[2]

Comparison between the Boussinesq and anelastic methods, along with a summary of the significant findings, appears in Chapter 6. Appendix A outlines the method of Frobenius and its application to the Taylor-Goldstein equation and its anelastic analog. In Appendix B the thermodynamic tools necessary to convert atmospheric data into buoyancy frequency and density scale height profiles are discussed and the algorithms used to perform the conversions presented.

[1]This work has been published by Nault and Sutherland (2007)
[2]This work is in preparation for submission to *J. Atmos. Sci.*

Chapter 2

Boussinesq Numerical Methods

2.1 Introduction

This section develops the theoretical and numerical tools necessary to model the propagation of small-amplitude two-dimensional internal gravity waves through a non-rotating, inviscid Boussinesq fluid. In the Boussinesq approximation density variations are assumed to be sufficiently small that they may be ignored in non-buoyancy terms. This approximation is therefore well suited to fluids with densities that do not change significantly over the extent of their domain, such as water in the ocean or air in the atmosphere over distances less than 8 km, a characteristic scale height. In Chapter 4 the Boussinesq approximation will be dropped and fluids that undergo significant density changes over their domain, such as air in the atmosphere over distances larger than 8 km, will be considered.

In section 2.2 the Taylor-Goldstein equation, which describes Boussinesq internal waves, is derived from the Navier-Stokes equations. The numerical tools required to solve the Taylor-Goldstein equation are then developed in section 2.3.1. A technique that determines the appropriate initial conditions and measures the relative transmission of the internal waves given specific

background profiles is presented in section 2.3.2.

2.2 Governing Equation

In the inviscid, Boussinesq approximation the equations of motion are

$$\rho_{00}\frac{\partial \boldsymbol{v}}{\partial t} + \rho_{00}\left(\boldsymbol{v}\cdot\nabla\right)\boldsymbol{v} = -\nabla p - g\rho\hat{\boldsymbol{z}}, \tag{2.1a}$$

$$\frac{\partial \rho}{\partial t} + \boldsymbol{v}\cdot\nabla\rho = 0, \tag{2.1b}$$

$$\nabla\cdot\boldsymbol{v} = 0, \tag{2.1c}$$

where $\boldsymbol{v} = (u, v, w)$ is the velocity field, p is the local pressure in the fluid, ρ is the local density of the fluid, and ρ_{00} is a characteristic fluid density.

In this study it is assumed that the waves are two dimensional and that there is no mean vertical flow. As such, the velocity field may be decomposed into a time-independent background, denoted by a bar over the z-dependent variable, and time-dependent perturbed component, denoted by a tilde over the variable:

$$u\left(x,y,z,t\right) = \bar{U}\left(z\right) + \tilde{u}\left(x,z,t\right), \tag{2.2a}$$

$$v\left(x,y,z,t\right) = 0, \tag{2.2b}$$

$$w\left(x,y,z,t\right) = 0 + \tilde{w}\left(x,z,t\right). \tag{2.2c}$$

Likewise, the density may be decomposed into a sum of background and perturbed contributions:

$$\rho\left(x,y,z,t\right) = \bar{\rho}\left(z\right) + \tilde{\rho}\left(x,z,t\right). \tag{2.3}$$

Substituting decompositions (2.2) and (2.3) into the momentum equation (2.1a) and eliminating nonlinear terms (as these are assumed to be small am-

plitude waves), a coupled linear system of equations is found:

$$\left(\partial_t + \bar{U}\partial_x\right)\tilde{u} + \bar{U}'\tilde{w} = -\frac{p_x}{\rho_{00}}, \tag{2.4a}$$

$$\left(\partial_t + \bar{U}\partial_x\right)\tilde{w} = -\frac{p_z}{\rho_{00}} - g\frac{\rho}{\rho_{00}}, \tag{2.4b}$$

where subscripts t, x, and z indicate partial differentiation with respect to the corresponding indices and primes indicate differentiation with respect to z.

As $v = 0$ everywhere in the flow, it is possible to define the streamfunction $\psi(x, z)$ as

$$(\tilde{u}, \tilde{w}) = \left(\frac{\partial\psi}{\partial z}, -\frac{\partial\psi}{\partial x}\right) \tag{2.5}$$

so that equation (2.1c) is satisfied. Substituting the streamfunction into equation (2.4), the perturbed velocities are eliminated:

$$\left(\partial_t + \bar{U}\partial_x\right)\psi_z - \bar{U}'\psi_x = -\frac{p_x}{\rho_{00}}, \tag{2.6a}$$

$$-\left(\partial_t + \bar{U}\partial_x\right)\psi_x = -\frac{p_z}{\rho_{00}} - g\frac{\rho}{\rho_{00}}. \tag{2.6b}$$

Applying the variable decompositions to equation (2.1b), it is required that

$$\left(\partial_t + \bar{U}\partial_x\right)\tilde{\rho} = \psi_x\bar{\rho}'. \tag{2.7}$$

The pressure terms may be eliminated from (2.6) by taking the partial derivative with respect to z of equation (2.6a) and subtracting from it the partial derivative with respect to x of equation (2.6b):

$$\left(\partial_t + \bar{U}\partial_x\right)\left(\psi_{xx} + \psi_{zz}\right) - \bar{U}''\psi_x = -g\frac{\tilde{\rho}_x}{\rho_{00}}. \tag{2.8}$$

Operating on this equation with $\left(\partial_t + \bar{U}\partial_x\right)$, then substituting in the partial derivative with respect to x of equation (2.7) the perturbed density is eliminated:

$$\left(\partial_t + \bar{U}\partial_x\right)^2\left(\psi_{xx} + \psi_{zz}\right) - \left(\partial_t + \bar{U}\partial_x\right)\bar{U}''\psi_x = -g\frac{\bar{\rho}'}{\rho_{00}}\psi_{xx}. \tag{2.9}$$

It is assumed the waves are horizontally periodic with fixed absolute frequency, so that the streamfunction may be decomposed into a periodic component multiplied by a z-dependent amplitude envelope, $\phi(z)$:

$$\psi(x,z,t) = \phi(z)\, e^{i(kx-\omega t)}, \tag{2.10}$$

where it is understood that the real valued component of the streamfunction is used when calculating physical properties of the flow. Introducing this decomposition into equation (2.9) the governing equation is found:

$$\bar{\Omega}^2\left(-k^2\phi+\phi''\right)+\bar{\Omega}\bar{U}''k\phi-k^2g\frac{\vec{\rho}'}{\rho_{00}}\phi=0 \tag{2.11}$$

where the Doppler shifted frequency, $\bar{\Omega}$, is defined as in equation (1.2). Introducing the squared buoyancy frequency, N^2, as defined in equation (1.3), equation (2.11) is further simplified:

$$\phi''+k^2\left(\frac{N^2}{\bar{\Omega}^2}+\frac{\bar{U}''}{k\bar{\Omega}}-1\right)\phi=0. \tag{2.12}$$

This is the Taylor-Goldstein equation (Drazin and Reid, 1981). Given values of ϕ and ϕ' at some fixed vertical location z_0, it is possible to integrate equation (2.12) and so determine ϕ everywhere. In the following discussion z_0 is considered the lower boundary of the domain and numerical integration propagates ϕ solutions upwards. For systems where physical waves propagate downwards z_0 may be considered the top of the domain – the two systems are equivalent in the Boussinesq approximation.

For fluid with uniform background flow $\bar{U}(z) = U_0$ and constant buoyancy frequency $N(z) = N_0$ the Taylor-Goldstein equation has solutions of the form

$$\phi(z) = e^{\pm imz}, \tag{2.13}$$

in which the dispersion relation for Boussinesq internal waves,

$$\Omega_0 = N_0\frac{k}{\sqrt{k^2+m^2}}, \tag{2.14}$$

implicitly defines m in terms of Doppler shifted frequency $\Omega_0 = \omega - kU_0$, N_0 and k. The vertical wavenumber, m, is real only if $\Omega_0 \leq N_0$. By convention m is defined to be positive and the $\pm$ sign in equation (2.13) establishes whether the waves propagate upwards or downwards.

2.3 Numerical Tools Overview

In this section the numerical tools required to solve equation (2.12) along with the techniques needed to determine the appropriate initial conditions are developed. A discussion of the appropriate measure of transmitted wave amplitude is also presented.

2.3.1 Numerical Solver

Numerical integration of the Taylor-Goldstein equation is performed using Stoermer's rule (Press et al., 1993) wherever $\bar{\Omega}$ is sufficiently large. Near a critical layer $\bar{\Omega}$ is close to zero and the Stoermer method fails, the method of Frobenius is applied in these regions. Indeed, if the gradient Richardson number,

$$\mathrm{Ri_g}(z) \equiv \frac{N^2(z)}{\left(\bar{U}'(z)\right)^2}, \tag{2.15}$$

exceeds $1/4$ at the critical level, ray theory suggests the waves asymptotically approach the level, neither reflecting nor transmitting across it (Lighthill, 1978). Although a more rigorous treatment of linear theory allows for transmission across a critical layer with $\mathrm{Ri_g} > 1/4$, waves near the singularity develop rapid vertical oscillations which lead to efficient wave dissipation. Thus when a critical layer is encountered solutions are found only in circumstances for which $\mathrm{Ri_g}$ is locally less than $1/4$.

Whenever the coefficient in parenthesis that precedes the ϕ term in equation (2.12) is greater in magnitude than 10^4 the numerical solver jumps over the singularities using the approximate analytic solution found by the method of Frobenius (see Appendix A). The solver then continues integrating using the Stoermer method.

An explicit iterative solver is developed using Stoermer's rule on the Taylor-Goldstein equation. The vertical domain is discretized into $N+1$ points as

$$z = z_0,\ z_1,\ \ldots,\ z_N. \tag{2.16}$$

The Taylor-Goldstein equation rewritten in discrete form is

$$\phi_n'' + b_n \phi_n = 0, \tag{2.17}$$

in which $n \in 0,\ \ldots,\ N$, $\phi_n \equiv \phi(z_n)$ and b_n is found from the background buoyancy frequency and horizontal shear profiles at $z = z_n$:

$$b_n = k^2 \left(\frac{N_n^2}{\bar{\Omega}_n^2} + \frac{\bar{U}_n''}{k\bar{\Omega}_n} - 1 \right). \tag{2.18}$$

Applying Stoermer's rule, ϕ_n is found as

$$\phi_{n+1} = \phi_n + \Delta_n \tag{2.19}$$

where

$$\Delta_n = \Delta_{n-1} - h_n^2 b_n \phi_n, \tag{2.20}$$

for $n \in 1,\ \ldots,\ N$ with $h_n = z_n - z_{n-1}$. At the first gridpoint

$$\Delta_0 = h_0 \left(\phi_0' - \frac{1}{2} h_1 b_0 \phi_0 \right) \tag{2.21}$$

so that if $\phi(z_0)$, $\phi'(z_0)$ and b_n are known ϕ_n may be iteratively computed.

2.3.2 Solution Driver

Using the iterative methods described above, initial ϕ and ϕ' values may be integrated over a vertical domain. However, appropriate choices of these boundary conditions remain to be found. By characterizing the streamfunction solutions at the top and bottom of the domains as a superposition of upward and downward propagating waves, physical arguments may be applied making the calculation of appropriate boundary conditions possible.

Over small regions at the boundaries of the domain the buoyancy frequency and shear profiles are artificially extended such that their values remain constant. This is equivalent to the assumption that the incident and reflected streamfunctions represent monochromatic plane waves and does not affect the behaviour of the internal waves. As such, at the bottom of the domain there is a finite region over which the Taylor-Goldstein equation has constant coefficients:

$$\phi'' + b_0\phi = 0. \tag{2.22}$$

Similarly, at the top of the domain there is a region where

$$\phi'' + b_N\phi = 0. \tag{2.23}$$

Equations (2.22) and (2.23) have analytic solutions

$$\phi_k(z) = C_k^+ e^{im_k z} + C_k^- e^{-im_k z}, \tag{2.24}$$

where $k = 0, N$ represents solutions at the bottom and top of the domains, respectively, C_k^+ and C_k^- are unknown wave amplitudes, and $m_k = \sqrt{b_k}$ are vertical wavenumbers. As the wavelike solutions at the beginning and end of the vertical domain is a requirement for the numerical solver, the vertical wavenumbers must be real valued, thus it is required that

$$b_k > 0 \tag{2.25}$$

for both $k = 0$ and $k = N$.

Near the bottom of the domain the streamfunction is written explicitly as

$$\phi_0(z) = \underbrace{A^+ e^{im_0 z}}_{\text{incident}} + \underbrace{A^- e^{-im_0 z}}_{\text{reflected}}. \tag{2.26}$$

Physically, this is the superposition of an upward-propagating incident wave and a downward-propagating reflected wave. Given the (generally complex) wave amplitudes A^+ and A^-, ϕ_0 may be calculated directly using equation (2.26). Furthermore, ϕ_0' may be calculated as:

$$\phi_0' = A^+ i m_0 e^{im_0 z_0} - A^- i m_0 e^{-im_0 z_0}. \tag{2.27}$$

Thus, using equations (2.26) and (2.27), the initial conditions required for the numerical solver are determined. The problem of finding the initial conditions has been reduced to the problem of finding appropriate incident and reflected wave amplitudes.

At the top of the domain the streamfunction solution may be written as

$$\phi_N(z) = \underbrace{B^+ e^{im_N z}}_{\text{outgoing}} + \underbrace{B^- e^{-im_N z}}_{\text{returning}}, \tag{2.28}$$

where B^+ is the outgoing wave amplitude and B^- is the returning wave amplitude. Physically, the outgoing wave represents wave energy that escapes through the top of the domain whereas the returning wave represents wave energy originating from beyond the top of the domain and propagating downwards. By causality the returning wave is unphysical. It is through the elimination of the returning wave that proper incident and reflected wave coefficients, and thus initial conditions, are selected.

Differentiating equation (2.28), ϕ_N' is found in terms of the outgoing and reflected wave amplitudes

$$\phi_N' = B^+ i m_N e^{im_N z_N} - B^- i m_N e^{-im_N z_N}. \tag{2.29}$$

As ϕ_N and ϕ'_N are known and unknowns B^+ and B^- are required to determine appropriate initial conditions, equations (2.28) and (2.29) must be used to find the desired quantities. Defining $\delta \equiv \cos(m_N z_N)$ and $\gamma \equiv \sin(m_N z_N)$, wave amplitudes B^+ and B^- are calculated from the final streamfunction values:

$$\begin{bmatrix} \mathrm{Re}\{B^+\} \\ \mathrm{Im}\{B^+\} \\ \mathrm{Re}\{B^-\} \\ \mathrm{Im}\{B^-\} \end{bmatrix} = \frac{1}{2m_N} \begin{bmatrix} m_N\delta & m_N\gamma & -\gamma & \delta \\ -m_N\gamma & m_N\delta & -\delta & -\gamma \\ m_N\delta & -m_N\gamma & -\gamma & -\delta \\ m_N\gamma & m_N\delta & \delta & -\gamma \end{bmatrix} \begin{bmatrix} \mathrm{Re}\{\phi_N\} \\ \mathrm{Im}\{\phi_N\} \\ \mathrm{Re}\{\phi'_N\} \\ \mathrm{Im}\{\phi'_N\} \end{bmatrix}. \tag{2.30}$$

So, given incident and reflected wave amplitudes A^+ and A^-, respectively, outgoing and returning wave amplitudes B^+ and B^-, respectively, may be calculated.

As discussed above, the appropriate choice of incident and reflected wave amplitudes will result in only outgoing, and not returning, waves at the top of the domain. Thus a choice of A^+ and A^- is sought that, upon integration, yields $B^- = 0$. To find A^+ and A^- such that $B^- = 0$ two sets of unique 'guesses' for the incident and reflected wave amplitudes are made and the subsequent outgoing and returning wave amplitudes are found and then superimposed to find a solution with $B^- = 0$. This process is illustrated schematically in Figure 2.1. An initial guess for the incident (labelled A_1^+) and reflected (labelled A_1^-) wave amplitudes is made. The system is then integrated and outgoing (labelled B_1^+) and returning (labelled B_1^-) wave amplitudes are found. The process is repeated for new incident wave amplitude guesses A_2^+ and A_2^-, which results in outgoing wave amplitude B_2^+ and returning wave amplitude B_2^-. As the system is linear, the two initial guesses may be superimposed to eliminate B^- and thus remove downward propagating waves at the top of the domain, this is illustrated in Figure 2.1*c*. Explicitly, the appropriate choices

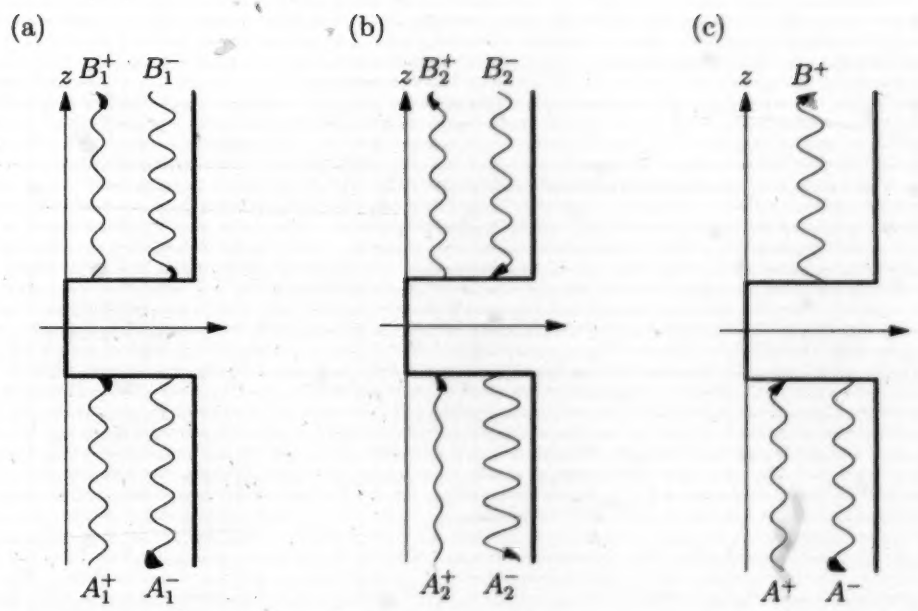

Figure 2.1: Schematic illustration of how solutions are superimposed to generate transmission coefficients. (*a*) Incoming and reflected wave amplitudes A_1^+ and A_1^- are arbitrarily selected, outgoing and returning wave amplitudes B_1^+ and B_1^- are calculated. (*b*) Different arbitrary amplitudes A_2^+ and A_2^- are selected, and B_2^+ and B_2^- are found. (*c*) By superimposing the first two solutions, correct amplitudes A^+ and A^- are calculated such that $B^- = 0$ resulting in transmitted amplitude B^+ and no downward propagating wave incident from above.

for A^- and A^+ are given by

$$A^+ = \frac{A_1^+}{B_1^-} - \frac{A_2^+}{B_2^-} \tag{2.31a}$$

$$A^- = \frac{A_1^-}{B_1^-} - \frac{A_2^-}{B_2^-}. \tag{2.31b}$$

Using this technique the appropriate initial conditions are found and the vertical structure of the internal waves completely described.

2.4 Transmission Quantification

Using the tools outlined in the previous section, for a prescribed incident amplitude, A^+, reflected and transmitted wave amplitudes A^- and B^+ are found. To analyze effectively the magnitude of internal wave transmission a non-dimensional measure of the degree of wave transmission, henceforth referred to as the 'transmission coefficient', is sought. In the absence of shear, the transmission coefficient is defined as the ratio of squares of the transmitted to incident amplitude:

$$T = \left| \frac{B^+}{A^+} \right|^2 \tag{2.32}$$

(Sutherland and Yewchuk, 2004). This is equivalent to the ratio of transmitted to incident energy density associated with the waves,

$$E = \left(k^2 + m^2\right) |A_\psi|^2 , \tag{2.33}$$

for waves with streamfunction amplitude A_ψ. Likewise the reflection coefficient is defined by

$$R = \left| \frac{A^-}{A^+} \right|^2 . \tag{2.34}$$

By conservation of energy, $T + R = 1$ must be satisfied.

In the presence of a mean horizontal background flow, wave energy is not conserved due to interactions between the Reynolds stress and the background

shear (Brown and Sutherland, 2007). For small amplitude waves, the appropriate corresponding conserved quantity is wave action (Lighthill, 1978; Eliassen and Palm, 1961), $\mathcal{A} = E/\Omega$. Equivalently, as derived using the methods of Hamiltonian fluid mechanics, the so-called pseudoenergy (Andrews and McIntyre, 1978; Scinocca and Shepherd, 1992) of internal waves

$$\mathcal{E} = \frac{\omega E}{\bar{\Omega}} = \omega \mathcal{A} \tag{2.35}$$

is conserved. As the wave solutions are in steady state, it is required that pseudoenergy not build up in the domain over time. As such, the transmitted pseudoenergy flux

$$\mathcal{F}_{\mathcal{E}} = \mathcal{E} c_{gz} \tag{2.36}$$

must equal the sum of the pseudoenergy flux of the incident and reflected waves. Here c_{gz} is the vertical group velocity given by

$$c_{gz} = -\frac{\bar{\Omega} m}{k^2 + m^2}. \tag{2.37}$$

Thus, for Boussinesq waves in general, the transmission coefficient is defined as:

$$T = \frac{\mathcal{F}_1}{\mathcal{F}_0} = \left| \frac{B^+}{A^+} \right|^2 \frac{m_1}{m_0}. \tag{2.38}$$

The reflection coefficient is defined as in equation (2.34). In the special case in which $m_1 = m_0$, equation (2.38) reduces to equation (2.32).

Brown and Sutherland (2007) developed an analytic solution for internal wave propagation across a piecewise-linear shear layer coincident with a buoyancy frequency gap. In their analysis of wave propagation they define transmission and reflection coefficient as in equations (2.38) and (2.34), respectively. They found that $T + R = 1$ independent of incident frequency and wavenumber, confirming that pseudoenergy flux is the correct measure of wave transmission.

Chapter 3

Boussinesq Simulations

3.1 Introduction

In this section the numerical methods outlined in the previous chapter are applied to several physical background buoyancy frequency and shear profiles. In section 3.2 the numerical solver is applied to profiles for which analytic measures of transmission are available. Comparing the numerical results to the analytic results, the validity of the code is established. The numerical solver is then applied to a diffuse buoyancy frequency step with stationary background flow in section 3.3 and the resulting transmission characteristics compared to heuristic arguments provided by WKB theory. The background flow is introduced in section 3.4 and the effects of critical layers analyzed. Finally, in section 3.5 the transmission characteristic of a mixed shear layer is found for varying horizontal shear strengths. These numerically generated profiles closely model unstable shear layers that are common to the ocean.

3.2 Code Testing

Using the numerical methods outlined in Chapter 2 a computer code was developed to calculate transmission coefficients. The code was tested by com-

paring numerically computed transmission coefficients with analytic results for an N^2-barrier in stationary fluid (Sutherland and Yewchuk, 2004) and in piecewise-linear shear (Brown and Sutherland, 2007). Integrating over 1000 gridpoints, a typical desktop computer requires about 1 second of computation time per gigahertz of processor clock rate to calculate the transmission coefficient for a single set of parameters. Examining transmission for a large range of $\omega - k$ space at high (300×300) resolution takes about a day. Typical deviations between the analytic and numerical results were negligible with maximum transmission coefficient discrepancy less than 1% over a broad range of input ω and k except when critical layers were encountered in which case deviations between the results were up to only 5%. The larger discrepancy can be explained by the approximations introduced by the method of Frobenius. The error can be improved by increasing the resolution of the numerical integration at the cost of computation time.

3.3 Stationary Fluid Results

The study of internal wave transmission is first restricted to a non-uniformly stratified but stationary fluid. The buoyancy frequency profile is

$$N^2(z) = \frac{N_1^2 - N_0^2}{2} \tanh\left(\frac{z}{L}\right) + \frac{N_0^2 + N_1^2}{2}, \tag{3.1}$$

as illustrated in Figure 3.1a. Internal waves originating from $z_0 \ll 0$, where $N \approx N_0$, and travelling upwards past the step to $z = z_1 \gg 0$, where $N \approx N_1$ are considered.

WKB theory at leading order predicts perfect transmission if $\omega < N_1$ and no transmission if $\omega > N_1$. The transmission coefficient is calculated for a range of nondimensional frequencies $\hat{\omega} = \omega/N_1$ and nondimensional horizontal wavenumbers $\hat{k} = kL$ in circumstances for which $\Lambda \equiv N_1^2/N_0^2 = 0.5$ and

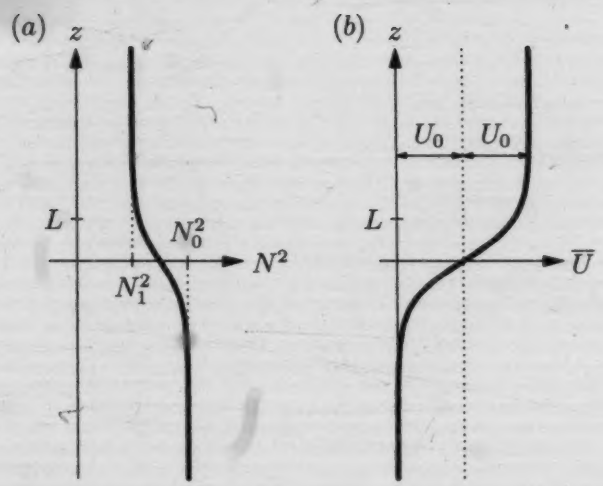

Figure 3.1: (a) Schematic illustration of the squared buoyancy frequency profile used for analysis in Section 3.3. $\overline{U} = 0$ in this case. (b) schematic illustration of the background horizontal flow used for analysis in Section 3.4. $N^2 = N_0^2$ in this case.

0.05. The corresponding computed transmission coefficients are plotted in Figure 3.2. The transition between the WKB and non-WKB regime is illustrated by lines of constant nondimensional transmitted vertical wavenumber $\hat{m}_1 \equiv m_1 L = 1$ and $1/8$, as determined from the dispersion relation for Boussinesq internal waves:

$$\hat{\omega} = \frac{\hat{k}}{\sqrt{\hat{k}^2 + \hat{m}_1^2}}. \tag{3.2}$$

Consistent with the WKB approximation, near-perfect transmission is observed for $\hat{m}_1 \gg 1$. Surprisingly, the approximation is satisfactory even for $\hat{m}_1 \approx 1$ corresponding to a transition depth, L, approximately $1/6$ of the vertical wavelength of the transmitted waves. Significant departure from the approximation occurs for $\hat{m}_1 \lesssim 1/8$.

In the limit as $L \to 0$ the smooth profile becomes a step at $z = 0$ and the transmission coefficient is found analytically using matching conditions at the

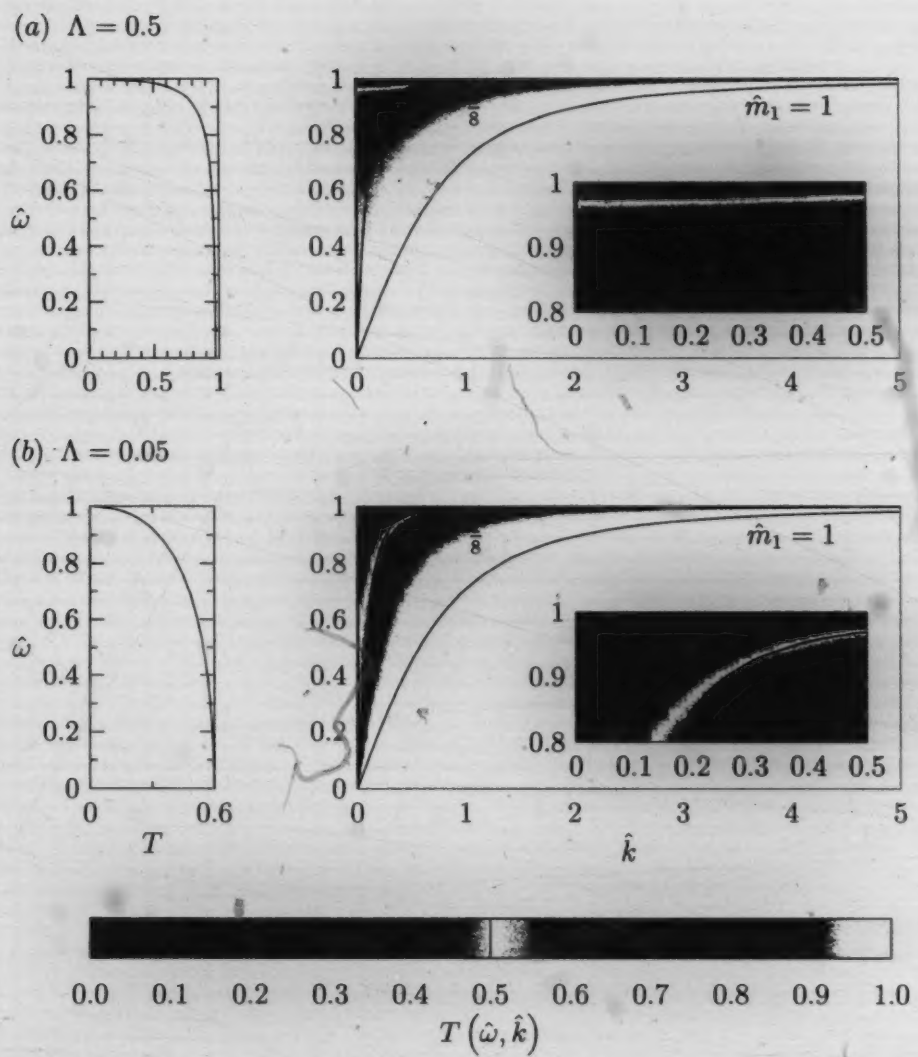

Figure 3.2: Transmission coefficient, T, as a function of incoming wave frequency scaled by incident buoyancy frequency, and wavenumber scaled by characteristic transition length for (a) $N_1^2 = 0.5$ and (b) $N_1^2 = 0.05$. Right plots show contours of T for a range of $\tilde{\omega}$ and $\tilde{k}$. Insert shows close-up of transmission for large frequency and small wavenumber. Left plots show analytic solution as $\tilde{k}$ tends to zero.

step:

$$T = \left[1 + \frac{1}{4}\left(\sqrt[4]{\frac{\frac{1}{\Lambda} - \hat{\omega}^2}{1 - \hat{\omega}^2}} - \sqrt[4]{\frac{1 - \hat{\omega}^2}{\frac{1}{\Lambda} - \hat{\omega}^2}}\right)^2\right]^{-1} \tag{3.3}$$

(Sutherland and Yewchuk, 2004; Brown and Sutherland, 2007; Drazin and Reid, 1981). This is plotted in the left panels of Figure 3.2. Comparing the analytic results to those found numerically for $\hat{k} \approx 0$ excellent agreement is found.

Comparing the transmission contour plots for $\Lambda = 0.5$ and 0.05, there is a clear trend: decreasing Λ decreases the relative transmission for fixed $\hat{m}_1$. As Λ is reduced, the contours of constant T approach lines of constant $\hat{m}_1$ for sufficiently large $\hat{k}$. For example, Figure 3.2*b* shows that the $\hat{m}_1 = 1/8$ contour closely corresponds to $T \approx 0.5$ for a range of $\hat{k} > 0$. Thus wave propagation into weakly stratified fluid is strongly dependent on the transmitted wave vertical wavenumber.

3.4 Shear Results

In this section the effects of background shear in the transmission of internal waves across a region of constant density gradient are examined. In this study the background shear is:

$$\bar{U}(z) = U_0 \tanh\left(\frac{z}{L}\right) + U_0, \tag{3.4}$$

and the buoyancy frequency is constant: $N^2(z) = N_0^2$. The background shear profile is drawn schematically in Figure 3.1*b*. The strength of the shear relative to the buoyancy frequency is described by the bulk Richardson number,

$$\mathrm{Ri_b} \equiv \left(\frac{N_0 L}{U_0}\right)^2. \tag{3.5}$$

The relevant physical parameters are nondimensional frequency, $\hat{\omega} = \omega/N_0$; horizontal wavenumber, $\hat{k} = kL/\sqrt{\mathrm{Ri_b}}$; vertical wavenumber, $\hat{m} = mL$; depth, $\hat{z} = z/L$; background shear, $\hat{U} = \bar{U}/U_0$; buoyancy frequency, $\hat{N} = N/N_0$; and Doppler-shifted frequency, $\hat{\Omega} = \bar{\Omega}/N_1$.

Here the focus is upon values of $\mathrm{Ri_b}$ lying in the range $0 < \mathrm{Ri_b} \leq 1$. In Section 3.5, transmission coefficients that are computed for background profiles resulting from the nonlinear evolution of the unstable flow are similar to those computed in this section. This suggests that the evolution of the shear layer has negligible influence upon wave propagation across the layer.

In each of the four cases considered ($\mathrm{Ri_b} = 0.001, 0.01, 0.1$, and 1) the gap width and maximum shear strength are $L = 1$ and $U_0 = 1$, respectively. The resulting transmission coefficients, over the range of all frequency and wavenumber that allow wavelike propagation, are illustrated in Figure 3.3. Requiring propagating waves at $\hat{z}_0$, $\hat{\omega} \leq 1$ is required. The plots are divided into four regions: to the left of the leftmost dashed line (where $\hat{\Omega}(\hat{z}_1) = \hat{\omega} - 2\hat{k} = 1$) and to the right of the rightmost dashed line (where $\hat{\Omega}(\hat{z}_1) = -1$) the Doppler-shifted frequency exceeds the buoyancy frequency at $\hat{z}_1 \gg 0$, and so propagation is not possible. The region between the leftmost dashed line and the dashed-dotted line (where $\hat{\Omega}(\hat{z}_1) = 0$) corresponds to wavenumber and frequency pairs that do not encounter critical layers anywhere in the flow. The corresponding horizontal phase speed is either negative (for $\hat{k} < 0$) or greater than $2U_0$ (for $\hat{k} > 0$). In region to the right of the dashed-dotted line the frequency and wavenumber of the internal waves are such that they encounter a critical layer. If $\mathrm{Ri_g} > 1/4$ at the critical level the waves exhibit a rapidly oscillating vertical structure. Consistent with the predictions of ray theory, it is assumed that the waves dissipate in this circumstance and so neither

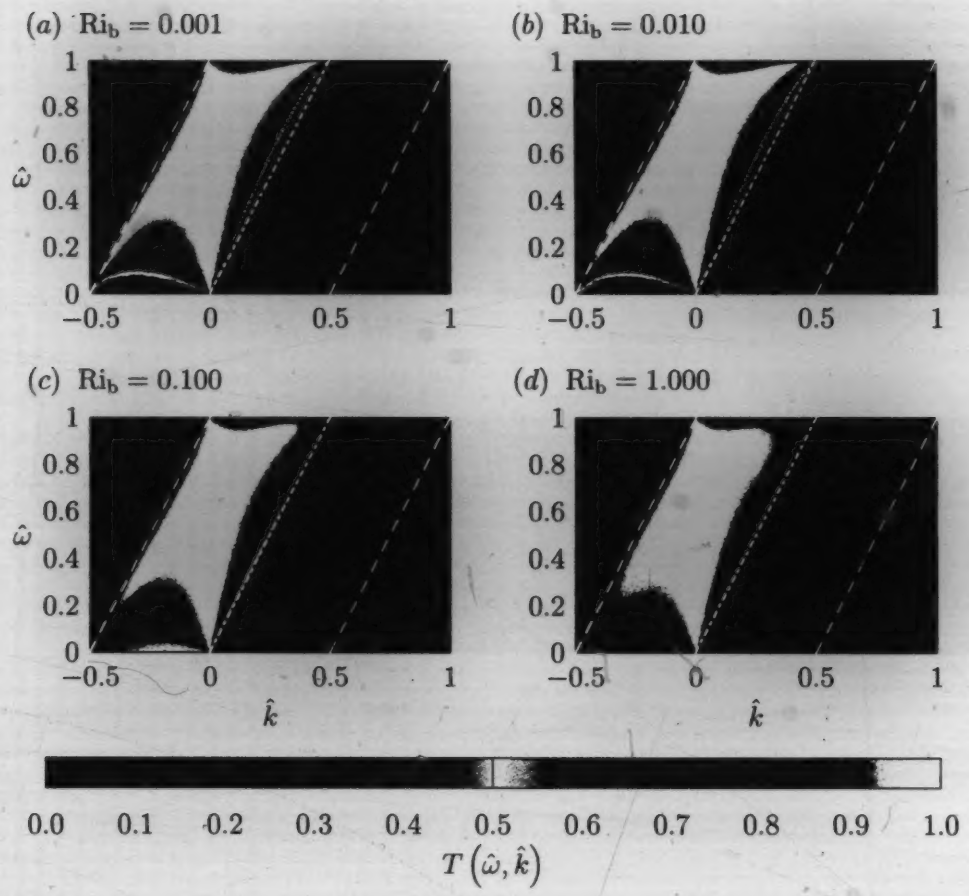

Figure 3.3: Transmission as a function of incoming wave frequency, scaled by N_0, and wavenumber, scaled by the root of the bulk Richardson number, for (*a*) $\mathrm{Ri_b} = 0.001$, (*b*) $\mathrm{Ri_b} = 0.010$, (*c*) $\mathrm{Ri_b} = 0.100$, and (*d*) $\mathrm{Ri_b} = 1.000$. To the left of the leftmost line and to the right of the rightmost dashed line wave propagation is not possible at large depths. The centre dashed-dotted line marks the boundary between waves that do not encounter a critical layer, to the left of the line, and waves that do encounter a critical layer, to the right of the line.

transmission nor reflection occurs.

The WKB approximation applies when $\hat{m} \gg 1$. The associated range of frequencies and wavenumbers lie in a small region above the line $\hat{\omega} = 2\hat{k}$, which corresponds to the dashed-dotted line in the four plots of Figure 3.3. Because the WKB approximation is plausible over such a small region this problem requires different techniques to completely describe wave propagation and is well-posed the numerical solver.

Figure 3.3*a* shows transmission coefficients for waves incident upon a highly unstable shear flow for which $\mathrm{Ri_b} = 0.001$. For $\hat{k} < 0$, despite being Doppler-shifted to frequencies close to N_0, transmission is strong for a wide range of $\hat{\omega}$ and $\hat{k}$. The transmission is lowest for small $\hat{\omega}$, corresponding to incident waves with vertical wavelengths that are short compared to the horizontal wavelength but long when compared with the gap depth. To the right of the dashed-dotted line, corresponding to parameters for which waves encounter a critical layer, there is weak but non-zero transmission over nearly the entire region.

In Figure 3.3*b*, the transmission coefficient is plotted for $\mathrm{Ri_b} = 0.01$. Although the bulk Richardson number has increased by an order of magnitude, N_0 is two orders of magnitude smaller than U_0/L so that shear effects still dominate. As such, the transmission is largely unchanged in the non-critical region. The most significant differences are apparent near $\hat{\omega} = 0$, where the transition from poor transmission to strong transmission occurs over a shorter range of $\hat{\omega}$, and also to the left of the dashed-dotted line that separates the region between critical and non-critical transmission, where the transition from weak transmission to strong transmission occurs over a smaller range of $\hat{k}$. In the critical region the effect of increasing $\mathrm{Ri_b}$ is more significant. There

is a smaller region of $\hat{\omega}$ and $\hat{k}$ which have $\mathrm{Ri}_g < 1/4$ at the critical layer so that the parameter range over which transmission occurs is smaller. However, because $\bar{\Omega}$ approaches zero at a critical layer, the $N^2/\bar{\Omega}^2$ term dominates the Taylor-Goldstein equation. As such, increasing N_0 by an order of magnitude significantly affects the transmission in the region that encounters a critical layer. Compared with the case where $\mathrm{Ri}_g = 0.001$, there is a large increase (typically over 500%) in the transmission coefficients in the critical region.

Figure 3.3*c* plots the transmission coefficient for $\mathrm{Ri}_b = 0.1$. In this case N_0 is the same order of magnitude as U/L, so the buoyancy frequency has significant influence on the transmission characteristics. Comparing the non-critical transmission region to that in Figures 3.3*a* and 3.3*b*, it is apparent that the transition from relatively weak to strong transmission near $\hat{\omega} = 0$ and the $\hat{\Omega}(z) = 0$ line occurs over a smaller range of frequencies – transmission coefficients are larger than 0.5 over nearly the entire domain. In the critical region transmission is even stronger. For smaller $\hat{\omega}$ and $\hat{k}$ the transmission coefficient is consistently as large as 0.3 and above 0.15 over most of the range of parameters with waves that encounter a critical level.

In Figure 3.3*d* transmission is plotted for relatively stable flow with $\mathrm{Ri}_b = 1$. In this case N_0 is the same order of magnitude as U/L and the shear has less impact upon the wave propagation. In the limit as Ri_b approaches infinity perfect transmission is expected throughout the non-critical region and no transmission is possible in the critical region. With $\mathrm{Ri}_b = 1$ the transmission is already approaching this limit with transmission greater than 0.95 over nearly the entire range of parameters that allow wave propagation. In the critical region, to the right of the dashed dotted line, transmission is not possible. This is because $\mathrm{Ri}_g > 1/4$ over the entire critical region so that waves may not

propagate across the critical layer.

3.5 Mixed Layer Results

The background profiles examined in the previous section are unstable for $\mathrm{Ri_g} < 1/4$. In this section wave transmission across a mixed layer resulting from taking the initial conditions given by equations (3.4) and (3.5) and solving the equations of motion so as to evolve the system until it reaches a quasi-steady state is considered. Explicitly, the horizontally averaged background N^2 and $\bar{U}$ profiles are determined at time $t = 100L/U_0$. The code used to perform this calculation is described in detail by Sutherland and Peltier (1992).

Background shear and buoyancy frequency profiles, as well as the gradient Richardson number in the central mixed region, are plotted in the left panels of Figure 3.4 for $\mathrm{Ri_b} = 0.001, 0.01$ and 0.1. The circumstance with $\mathrm{Ri_b} = 1$, studied in Section 3.4, is omitted as the flow is stable in this case. The evolution of the flow involves the development of Kelvin-Helmholtz billows that mix the region about $\hat{z} = 0$ both broadening the shear layer and locally reducing $\hat{N}$. The resulting mean flow and horizontal averaged $\hat{N}^2$ profiles are similar to the piecewise-linear profile across which transmission was considered using an analytic formula by Brown and Sutherland (2007). Not only do incident waves encounter a shear layer, but they also encounter a localized region of reduced $\hat{N}^2$ where the waves may be evanescent. If this region is sufficiently narrow, it is nonetheless possible for waves to tunnel through. The corresponding transmission coefficients are given in the right panels of Figure 3.4*a*, *b*, *c*. These are analogous to Figures 3.3*a*, *b*, and *c* respectively.

When the shear is relatively weak compared to the strength of the buoyancy frequency the resulting transmission is similar to that of the non-evolved

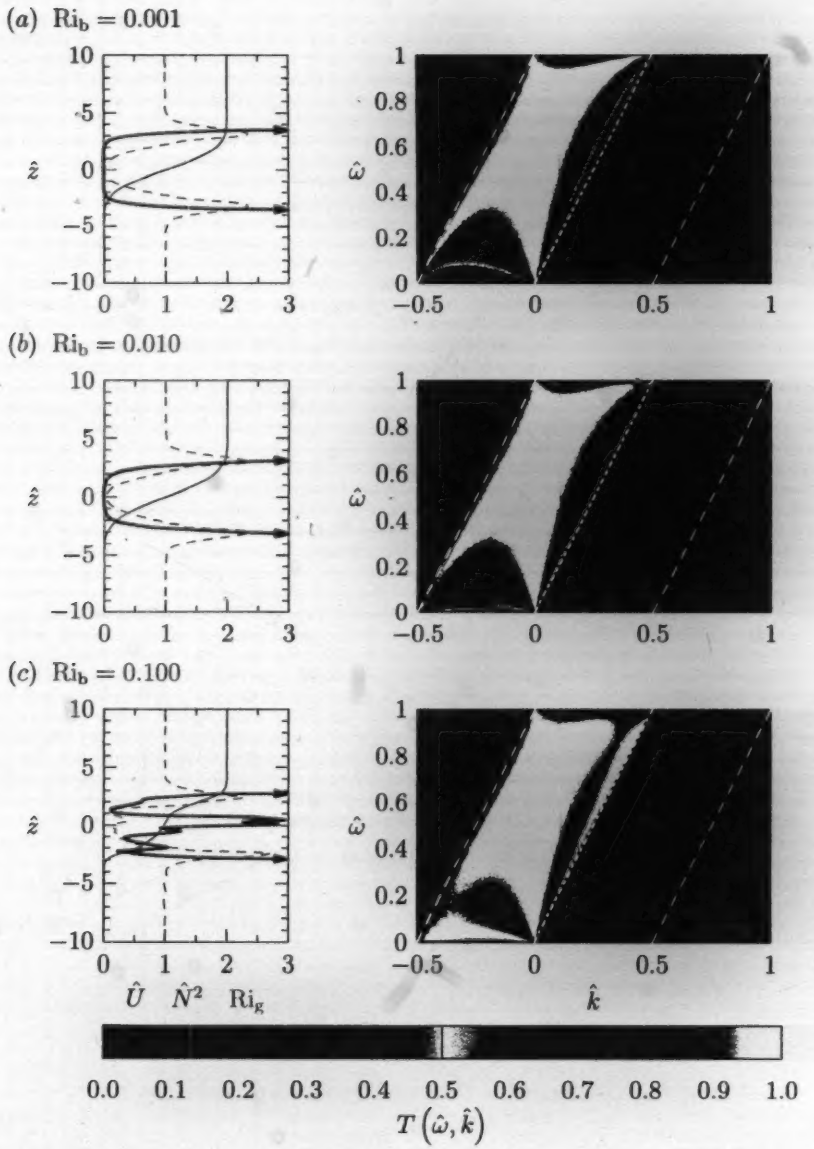

Figure 3.4: Background buoyancy frequency, shear, and gradient Richardson number profiles (left panels) for an evolving shear flow at $t = 100L/U_0$ and corresponding transmission contour plots (right panels) for (*a*) $\mathrm{Ri_b} = 0.001$, (*b*) $\mathrm{Ri_b} = 0.010$, and (*c*) $\mathrm{Ri_b} = 0.100$. The contour range and bounding lines correspond to those in Figures 3.3*a*, *b*, and *c*.

profiles in the non-critical region. As in Section 3.3 it is found that although there is a reflection level near $\hat{z} = 0$ where $\hat{N}^2 = 0$, almost perfect transmission occurs for a wide range of $\hat{\omega}$ and $\hat{k}$. The similarities between the transmission contours for the evolved and original profiles suggests that internal waves transmit across the mixed region throughout the mixing process.

In the region of the plot where a critical layer is encountered (to the right of the dashed-dotted line) there are more significant differences between the transmission contours for the original and evolved profiles. The mixing induces opposing effects in the gradient Richardson number: the broadening of the shear layer acts to reduce $\bar{U}'$, thus increasing $\mathrm{Ri_g}$, while the mixing reduces N, thus decreasing $\mathrm{Ri_g}$. Although the effects are comparable in magnitude, $\mathrm{Ri_g}$ is typically larger after the fluid has mixed suggesting that the mixing in the gap is dominated by the broadening of the shear layer. As such, wave transmission is possible for a smaller range of $\hat{\omega}$ and $\hat{k}$ and indeed the transmission coefficient is non-negligible over a smaller parameter range.

For $\mathrm{Ri_b} = 0.001$ the shear and buoyancy frequency profiles are symmetric about $\hat{z} = 0$. This results from the fine-scale convective instability which occurs when KH billows transport dense fluid over light. In the mixed region $\mathrm{Ri_g} < 1/4$ for $|\hat{z}| < 2.81$ and in this range $0.05 < \hat{U} < 1.95$. As such, transmission is possible in the critical region for a very broad range of $\hat{\omega}$ and $\hat{k}$. In comparing transmission for the evolved and non-evolved profiles of Figures 3.4*a* and 3.3*a*, respectively, it is clear that in the critical region transmission occurs over a comparable range of $\hat{\omega}$ and $\hat{k}$ and that transmission is poor in both cases - the differences between the two plots are almost indistinguishable.

For $\mathrm{Ri_b} = 0.01$ the differences between the original and evolved profiles are more apparent. Comparing Figures 3.3*b* and 3.4*b* it is clear that there

is generally stronger transmission of waves that do not encounter a critical level, particularly for low frequency waves. A transmission 'valley' occurs for $0 \lesssim \hat{\omega} \lesssim 0.1$ and $-0.5 < \hat{k} < 0$ when $0.1 \lesssim \hat{\omega}/\hat{k} \lesssim 0.5$. For these profiles, $\mathrm{Ri_g} < 1/4$ in the mixed region for $|\hat{z}| < 2.11$ over which range $0.18 < \hat{U} < 1.82$. In the critical region slightly stronger transmission occurs compared to that computed for the original profiles, although non-negligible transmission occurs over a smaller range of parameter space for the evolved profiles.

For $\mathrm{Ri_b} = 0.1$, comparing the transmission contours in Figures 3.3*c* and 3.4*c* it is again clear that, in the non-critical region, transmission is generally stronger for the evolved plots and that a transmission 'valley' (though weak) occurs for $0.5 \lesssim \hat{\omega}/\hat{k} \lesssim 2.3$ if $\hat{\omega} < 0.3$. In the critical region there is significant deviation from the transmission contours obtained from the original profiles. There are two small bands of (relatively weak) transmission for the evolved profiles whereas transmission was possible over a large range of parameters for the original profiles. The lower frequency transmission band coincides with waves encountering a critical level with $\mathrm{Ri_g} < 1/4$ where $-2.34 < \hat{z} < -2.19$ for which $0.42 < \hat{U} < 0.47$. There is a maximum in shear gradient at this level. The higher transmission band occurs for waves encountering a critical level where $1.02 < \hat{z} < 1.56$ for which $1.11 < \hat{U} < 1.31$. This is coincident with a minimum in buoyancy frequency. For the original profiles critical transmission was at its greatest in this case.

Chapter 4

Anelastic Numerical Methods

4.1 Introduction

In this section, the Boussinesq approximation made in previous sections is relaxed and the propagation of anelastic internal waves considered. In a liquid, the density does not change significantly over the depth so the Boussinesq approximation is valid. The Boussinesq approximation is therefore effectively applied when analyzing internal gravity waves in the ocean. In the atmosphere the density may change significantly over a vertical domain extending over tens of kilometres. In particular, the density decreases by approximately three orders of magnitude from the surface to the top of the stratosphere, at altitude $z \approx 50$ km, so the Boussinesq approximation is no longer valid.

The anelastic approximation is an extension of the Boussinesq approximation because it can effectively model internal waves in domains where the background density decreases significantly in the vertical. As internal waves propagate upwards, the background density decreases and the amplitude conversely must increase in order to conserve momentum. This characteristic increase in wave amplitude with altitude is referred to as 'anelastic growth'. In the derivation of the Taylor-Goldstein equation, a characteristic density, ρ_{00},

rather than the background density, $\bar{\rho}$, was used in the continuity equation (2.1c) and preceding the time derivatives in the momentum equations (2.4). As such, the physical effects of significant density change were neglected in the Boussinesq approximation.

An anelastic equivalent to the Taylor-Goldstein equation is derived by making simplifying approximations to the Navier-Stokes equations for an anelastic fluid. In the anelastic approximation it is assumed that background potential temperature varies slowly in the vertical (Lipps and Hemler, 1982). By considering only the background density in the continuity equation, the fastest time scale upon which fluid motions occur is set by internal gravity waves (Ogura and Phillips, 1962). In this sense, the anelastic approximation effectively filters sound waves from the full equations of motion. The resulting equations are examined and the numerical tools developed in Chapter 2 are modified to incorporate the exponential wave envelopes associated with anelastic waves. The numerical model developed in this section is then applied to the piecewise-linear shear and density profiles considered by Brown and Sutherland (2007) and atmospheric profiles observed over Jan Mayen, as considered by Eckermann et al. (2006).

4.2 Governing Equation

Scinocca and Shepherd (1992) present the most general form of the equations of motion in the anelastic approximation as developed by Batchelor (1953)

and Lipps and Hemler (1982):

$$\frac{\partial \boldsymbol{v}}{\partial t} + (\boldsymbol{v} \cdot \nabla)\,\boldsymbol{v} = -c_p \bar{\theta} \nabla\left(\tilde{\pi}\right) - c_p \frac{d\bar{\pi}}{dz} \tilde{\theta} \hat{\boldsymbol{z}}, \tag{4.1a}$$

$$\frac{\partial \tilde{\theta}}{\partial t} + (\boldsymbol{v} \cdot \nabla)\,\tilde{\theta} + w \frac{d\bar{\theta}}{dz} = 0, \tag{4.1b}$$

$$\nabla \cdot (\bar{\rho} \boldsymbol{v}) = 0. \tag{4.1c}$$

In addition to the velocity and density fields, $\boldsymbol{v}$ and ρ, the anelastic equations include the potential temperature, θ, and Exner pressure, π. The Exner pressure is a measure of pressure scaled by the ground level pressure p_{00}:

$$\pi = \left(\frac{p}{p_{00}}\right)^{\kappa}, \tag{4.2}$$

where

$$\kappa = \frac{R}{c_p} \approx \frac{2}{7}, \tag{4.3}$$

for gas constant $R = 0.28705$ kJ/K $\cdot$ kg and heat capacity at constant pressure $c_p = 1.0057$ kJ/K $\cdot$ kg for dry air.

The potential temperature is the equilibrium temperature a parcel of air would attain if moved adiabatically to ground level. Using the Exner pressure it is defined as

$$\theta = \frac{T}{\pi}, \tag{4.4}$$

for air at temperature T. In equations (4.1a) – (4.1c) the thermodynamic fields have been decomposed into background and perturbed parts:

$$\pi\left(x, z, t\right) = \bar{\pi}\left(z\right) + \tilde{\pi}\left(x, z, t\right), \tag{4.5a}$$

$$\theta\left(x, z, t\right) = \bar{\theta}\left(z\right) + \tilde{\theta}\left(x, z, t\right), \tag{4.5b}$$

$$\rho\left(x, z, t\right) = \bar{\rho}\left(z\right) + \tilde{\rho}\left(x, z, t\right). \tag{4.5c}$$

Wilhelmson and Ogura (1972) showed that if $\bar{\theta}$ is allowed to vary in the vertical, then the system prescribed by equations (4.1a) – (4.1c) may not

conserve energy. Lipps and Hemler (1982) suggest that equation (4.1a) may be replaced by

$$\frac{\partial \boldsymbol{v}}{\partial t} + (\boldsymbol{v} \cdot \nabla)\, \boldsymbol{v} = -\nabla \left(c_p \bar{\theta} \tilde{\pi} \right) - c_p \frac{d\bar{\pi}}{dz} \tilde{\theta} \hat{\boldsymbol{z}}, \tag{4.6}$$

without introducing greater approximation if $\bar{\theta}$ varies slowly in the vertical, a condition already required in the initial approximations used to derive the system. Using equations (4.6), (4.1b), and (4.1c) to model the system, an anelastic equivalent to the Taylor-Goldstein equation is found.

As in the derivation of the Taylor-Goldstein equation, it is assumed that there is no mean vertical flow and the waves are two dimensional. As such, the velocity field may be expressed as:

$$\boldsymbol{v} = \left(\bar{U}(z) + \tilde{u}(x,z,t), 0, \tilde{w}(x,z,t) \right). \tag{4.7}$$

Furthermore, only small amplitude waves are considered so all nonlinear terms may be neglected. Expanding into component form, applying equation (4.7), and linearizing, equation (4.6) becomes

$$\left(\partial_t + \bar{U} \partial_x \right) \tilde{u} + \bar{U}' \tilde{w} = -c_p \bar{\theta} \tilde{\pi}_x, \tag{4.8a}$$

$$\left(\partial_t + \bar{U} \partial_x \right) \tilde{w} = -c_p \left(\bar{\theta}' \tilde{\pi} + \bar{\theta} \tilde{\pi}_z + \bar{\pi}' \tilde{\theta} \right), \tag{4.8b}$$

where subscripts t, x and z indicate partial differentiation with respect to the corresponding indices and primes indicate differentiation with respect to z. Similarly applying the velocity field expansion to equation (4.1b) and linearizing gives

$$\left(\partial_t + \bar{U} \partial_x \right) \tilde{\theta} + \tilde{w} \bar{\theta}' = 0. \tag{4.9}$$

As the waves are two dimensional, from the continuity equation (4.1c) it is possible to define the mass flux streamfunction $\psi(x,z)$ such that

$$(\tilde{u}, \tilde{w}) = \left(\frac{1}{\bar{\rho}} \frac{\partial \psi}{\partial z}, -\frac{1}{\bar{\rho}} \frac{\partial \psi}{\partial x} \right) \tag{4.10}$$

is satisfied. As waves propagate vertically upwards the ambient background density decreases so that wave induced velocities typically increase. This is required for momentum conservation: as density decreases velocity must increase. Applying the mass flux streamfunction definition to equations (4.8a), (4.8b), and (4.9) the system becomes:

$$\frac{1}{\bar{\rho}}\left(\partial_t + \bar{U}\partial_x\right)\psi_z - \frac{\bar{U}'}{\bar{\rho}}\psi_x = -c_p\bar{\theta}\tilde{\pi}_x, \tag{4.11a}$$

$$\frac{1}{\bar{\rho}}\left(\partial_t + \bar{U}\partial_x\right)\psi_x = c_p\left(\bar{\theta}'\tilde{\pi} + \bar{\theta}\tilde{\pi}_z + \bar{\pi}'\tilde{\theta}\right), \tag{4.11b}$$

$$\left(\partial_t + \bar{U}\partial_x\right)\tilde{\theta} - \frac{1}{\bar{\rho}}\psi_x\bar{\theta}' = 0. \tag{4.11c}$$

The pressure terms are eliminated from the system by adding the partial derivative with respect to z of equation (4.11a) to the partial derivative with respect to x of equation (4.11b):

$$\left(\partial_t + \bar{U}\partial_x\right)\left(\psi_{zz} + \frac{1}{H_\rho}\psi_z + \psi_{xx}\right) - \left(\frac{\bar{U}'}{H_\rho} + \bar{U}''\right)\psi_x = c_p\bar{\rho}\bar{\pi}'\tilde{\theta}_x, \tag{4.12}$$

where H_ρ is defined by (1.1). The potential temperature variation term may then be eliminated by operating with $\left(\partial_t + \bar{U}\partial_x\right)$ on equation (4.12), then substituting the partial derivative with respect to x of equation (4.11c) multiplied by $c_p\bar{\rho}\bar{\pi}'$:

$$\left(\partial_t + \bar{U}\partial_x\right)^2\left(\psi_{zz} + \frac{1}{H_\rho}\psi_z + \psi_{xx}\right) - \left(\partial_t + \bar{U}\partial_x\right)\left(\frac{\bar{U}'}{H_\rho} + \bar{U}''\right)\psi_x = c_p\bar{\pi}'\bar{\theta}'\psi_{xx}. \tag{4.13}$$

Solutions are sought that are periodic both in time, having frequency ω, and in the horizontal space, having horizontal wavenumber k. The mass flux streamfunction is thus decomposed into a periodic component multiplied by a z-dependent amplitude envelope, $\phi(z)$:

$$\psi(x,z,t) = \phi(z)\, e^{i(kx-\omega t)}. \tag{4.14}$$

Again, it is understood that the real valued component of the streamfunction is considered when calculating the physical properties of the flow. Substituting this definition into equation (4.13) a second-order ordinary differential equation is found:

$$\bar{\Omega}^2\left(\phi'' + \frac{1}{H_\rho}\phi' - k^2\phi\right) + \bar{\Omega}k\left(\frac{1}{H_\rho}\bar{U}' + \bar{U}''\right)\phi - c_p k^2 \bar{\pi}'\bar{\theta}'\phi = 0, \tag{4.15}$$

where the Doppler shifted frequency is defined by equation (1.2).

Background hydrostatic balance requires

$$\bar{\theta}\frac{d\bar{\pi}}{dz} = -\Gamma, \tag{4.16}$$

in which $\Gamma = g/c_p$ is the dry adiabatic lapse rate, so that equation (4.15) may be simplified further:

$$\phi'' + \frac{1}{H_\rho}\phi' + k^2\left(\frac{N_\theta^2}{\bar{\Omega}^2} + \frac{\bar{U}''}{k\bar{\Omega}} - 1 + \frac{\bar{U}'}{k\bar{\Omega}H_\rho}\right)\phi = 0, \tag{4.17}$$

where N_θ^2 is the potential temperature-based squared buoyancy frequency defined as in (1.4). A discussion of the relationship between potential temperature and background density scale height along with the thermodynamic tools required to convert between the two is presented in Appendix B. Equation (4.17) is the anelastic extension of the Taylor-Goldstein equation and will be referred to hereafter as the 'anelastic Taylor-Goldstein equation'.

For fluid with uniform background flow $\bar{U}(z) = U_0$ and exponentially decreasing density with scale height, H_ρ, the background buoyancy frequency is constant $N_\theta = N_0$ and the anelastic Taylor-Goldstein equation has solutions of the form

$$\phi(z) = e^{-z/2H_\rho}e^{\pm imz} \tag{4.18}$$

where vertical wavenumber, m, is defined implicitly by the dispersion relation

for anelastic internal waves,

$$\Omega = N_0 \frac{k}{\sqrt{k^2 + m^2 + \frac{1}{4H_\rho^2}}}. \tag{4.19}$$

In the Boussinesq limit the anelastic Taylor-Goldstein equation reduces to the Taylor-Goldstein equation. Explicitly, the Boussinesq limit is characterized by vertically varying density that does not change significantly over the length of the domain, L_d, requiring

$$L_d \left| \frac{d\bar{\rho}}{dz} \right| \ll \rho_{00}. \tag{4.20}$$

Substituting this requirement into the Boussinesq squared buoyancy frequency definition (1.3), the requirement becomes

$$L_d \ll H_\rho \tag{4.21}$$

so that terms in equation (4.17) involving H_ρ^{-1} may be negated in the Boussinesq limit. As such, the anelastic Taylor-Goldstein equation reduces to

$$\phi'' + k^2 \left(\frac{N_\theta^2}{\bar{\Omega}^2} + \frac{\bar{U}''}{k\bar{\Omega}} - 1 \right) \phi = 0, \tag{4.22}$$

which is the form Taylor-Goldstein equation given by (2.12).

4.3 Numerical Tools Overview

In this section an overview of the numerical tools used to model anelastic internal waves is presented. The results of section 2.3 are extended to include non-zero ϕ' coefficients, which arise in the anelastic system and introduce exponential decay in streamfunction magnitude in regions of constant buoyancy frequency and shear. In addition to the tools required to model anelastic internal waves, thermodynamic principles are needed to convert atmospheric profiles into buoyancy frequency and density scale height profiles. A discussion of this process is presented in Appendix B.

4.3.1 Numerical Solver

Stoermer's rule was used to solve the Taylor-Goldstein equation (2.12) but this method cannot be applied in the anelastic case due to the presence of the ϕ' term in (4.17). A more sophisticated and numerically intensive ordinary differential equation solver must be used to model anelastic internal wave propagation. Due to its relative simplicity, the Heun method (Press et al., 1993) is used to integrate over non-critical points in the domain. Near critical points, where the coefficient of the ϕ term becomes large, the method of Frobenius is again implemented (see Appendix A). As in the Boussinesq case, the Frobenius solver is implemented whenever the magnitude of the ϕ coefficient, scaled by the square of local discretization step size, is larger than 10^4.

The domain is discretized into $N+1$ points as in equation (2.16). Then the anelastic Taylor-Goldstein equation is rewritten in discrete form:

$$\phi_n'' + a_n \phi_n' + b_n \phi_n = 0, \tag{4.23}$$

in which $n \in 0, \ldots, N$, $\phi_n \equiv \phi(z_n)$ and the coefficients a_n and b_n are found from the background N_θ, H_ρ, and $\bar{U}$ profiles at $z = z_n$:

$$a_n = \frac{1}{H_{\rho_n}} \tag{4.24a}$$

$$b_n = \frac{N_{\theta_n}^2 k^2}{\bar{\Omega}_n^2} + \frac{\bar{U}_n'' k}{\bar{\Omega}_n} - k^2 + k \frac{\bar{U}_n'}{H_{\rho_n} \bar{\Omega}_n}. \tag{4.24b}$$

The second-order differential equation is then converted into a system of two first-order differential equations:

$$\boldsymbol{r}_n' = \begin{bmatrix} s_n' \\ t_n' \end{bmatrix} = \begin{bmatrix} t_n \\ -a_n t_n - b_n s_n \end{bmatrix} = \boldsymbol{f}(z_n, \boldsymbol{r}_n). \tag{4.25}$$

Equation (4.23) is recovered by setting $s_n = \phi_n$ and $t_n = \phi_n'$. Using this discrete formulation, the Heun method is applied to advance the equation

iteratively:

$$\boldsymbol{r}_{n+1} = \boldsymbol{r}_n + h_{n+1}\left(\boldsymbol{f}\left(z_n, \boldsymbol{r}_n\right) + \boldsymbol{f}\left(z_{n+1}, \boldsymbol{r}_n + h_{n+1}\boldsymbol{f}\left(z_n, \boldsymbol{r}_n\right)\right)\right), \tag{4.26}$$

where the not necessarily uniform step size $h_{n+1} = (z_{n+1} - z_n)/2$ has been introduced. Expanding equation (4.26), explicit formulae in terms of known quantities are found for the numerical integration

$$s_{n+1} = s_n + 2h_{n+1}t_n - a_n h_{n+1}^2 t_n - b_n h_{n+1}^2 s_n \tag{4.27a}$$

$$\begin{aligned} t_{n+1} = t_n &- h_{n+1}\left(a_n t_n + b_n s_n\right) - a_{n+1}h_{n+1}\left(t_n - h_{n+1}\left(a_n t_n + b_n s_n\right)\right) \\ &- b_{n+1}h_{n+1}\left(s_n + h_{n+1}t_n\right). \end{aligned} \tag{4.27b}$$

4.3.2 Solution Driver

As in the Boussinesq case, appropriate initial conditions are found through the superposition of two incorrect initial wave amplitude 'guesses'. However, the anelastic problem is complicated by the introduction of anelastic growth: in regions of constant buoyancy frequency and uniform flow, the streamfunction magnitude decays exponentially with height whereas in the Boussinesq case it remains constant.

To establish wave amplitudes, which are required to determine the appropriate initial conditions, a small region over which the coefficients of equation (4.23) remain constant is required at the bottom and top of the vertical domain. To this end, the numerical solver artificially extends the profiles at the boundaries of the domain holding the coefficients constant. This does not affect the transmission coefficient as the waves propagate freely in these regions. In a region about the beginning of the domain the anelastic Taylor-Goldstein equation has constant coefficients:

$$\phi'' + a_0\phi' + b_0\phi = 0, \tag{4.28}$$

where a_0 and b_0 are given by the discretization presented in equation (4.24). Likewise, in a region about the top of the profile, equation (4.17) is rewritten as

$$\phi'' + a_N\phi' + b_N\phi = 0. \tag{4.29}$$

For a second-order differential equation with constant coefficients in the form of equations (4.28) and (4.29), solutions are given by

$$\phi_k(z) = C_k^+ e^{zr_k^+} + C_k^- e^{zr_k^-}, \tag{4.30}$$

for yet-to-be-determined wave amplitudes C_k^+ and C_k^- where $k = 0, N$ represent the solutions at the bottom and top of the domain, respectively, and r_k^+ and r_k^- found as the roots to the indicial equation

$$r_k^2 + a_k r_k + b_k = 0, \tag{4.31}$$

so that explicitly

$$r_k^+ = -\frac{a_k}{2} + i\sqrt{b_k - \frac{a_k^2}{4}} \tag{4.32a}$$

$$r_k^- = -\frac{a_k}{2} - i\sqrt{b_k - \frac{a_k^2}{4}}. \tag{4.32b}$$

Solutions of (4.30) describe propagating waves whenever r_k^+ and r_k^- have an imaginary component. Requiring wavelike behaviour at the extremities of the vertical domain restricts the study to incident and transmitted waves having ω and k specified such that

$$b_k > \frac{a_k^2}{4} \tag{4.33}$$

for both $k = 0$ and $k = N$. Comparing this condition for wavelike behaviour to the Boussinesq equivalent, given by equation (2.25), it is clear that in the anelastic case the condition for wavelike solutions is more restrictive. In the Boussinesq case b_k need only be larger than zero for wavelike solutions whereas

now it must be larger than $a_k^2/4 > 0$. As the coefficient a_k appears only in the anelastic Taylor-Goldstein equation and typically becomes larger as scale height is reduced, the range of frequency and horizontal wavenumber over which transmission is possible is typically reduced as the flow becomes more anelastic.

The smaller range of valid frequency and wavenumber combinations that allow wavelike solutions may be explained by differences between the Boussinesq dispersion relation, (2.14), and the anelastic dispersion relation, (4.19). At the threshold between vertically propagating waves and non-wavelike solutions $m = 0$, so that for wavelike solutions in the anelastic case the dispersion relation requires

$$\frac{\Omega}{N} < \frac{k}{\sqrt{k^2 + \frac{1}{4H_\rho^2}}}. \tag{4.34}$$

In the Boussinesq case, for wavelike solutions it is required that

$$\frac{\Omega}{N} < \frac{1}{|k|}. \tag{4.35}$$

So as the flow becomes more anelastic, and H_ρ is decreased, the condition for wavelike solutions in the anelastic case becomes more restrictive and the range of frequency and wavenumber combinations that permit wavelike solutions reduced.

Near the bottom of the domain the streamfunction solution may be written as

$$\phi_0(z) = \underbrace{A^+ e^{-\sigma_0 z} e^{im_0 z}}_{\text{incident}} + \underbrace{A^- e^{-\sigma_0 z} e^{-im_0 z}}_{\text{reflected}}, \tag{4.36}$$

where $\sigma_0 = a_0/2$ and $m_0 = \sqrt{b_0 - a_0^2/4}$. Physically, equation (4.36) describes the superposition of an incident and reflected wave, each in an exponentially decreasing wave envelope. The incident wave amplitude A^+ is a measure of the strength of the waves generated at the source, where $z = 0$. The reflected

wave amplitude, A^-, measures the strength of the internal waves returning to the point of generation due to interactions between the waves and the atmosphere. Given the (generally complex) wave amplitudes A^+ and A^- it is then possible to calculate $\phi_0 = \phi(z_0)$ directly. Furthermore, $\phi_0' = \phi'(z_0)$ may also be calculated directly:

$$\phi'(z) = A^+(-\sigma_0 + im_0)e^{-\sigma_0 z}e^{im_0 z} - A^-(\sigma_0 + im_0)e^{-\sigma_0 z}e^{-im_0 z}. \quad (4.37)$$

Using equations (4.36) and (4.37), lower boundary conditions ϕ_0 and ϕ_0' are found, a combination of the Heun method and the method of Frobenius may then be used to calculate ϕ over the entire domain. All that remains to be found is an appropriate choice for incident and reflected wave amplitudes A^+ and A^-.

At the top of the domain the streamfunction is characterized as

$$\phi(z) = \underbrace{B^+e^{-\sigma_N z}e^{im_N z}}_{\text{outgoing}} + \underbrace{B^-e^{-\sigma_N z}e^{-im_N z}}_{\text{returning}}, \quad (4.38)$$

where $\sigma_N = a_N/2$ and $m_N = \sqrt{b_N - a_N^2/4}$ and B^+ and B^- are outgoing and returning wave amplitudes, respectively. Physically, the outgoing wave represents wave energy that escapes through the top of the domain. The returning wave is unphysical because it breaks causality: it suggests wave energy is entering the system from the top of the domain and moving downwards. In selecting the correct boundary conditions, this wave must be eliminated. As in equations (4.36) and (4.37), a relationship between ϕ_N and ϕ_N', and B^+ and B^- is found

$$\phi'(z) = B^+(-\sigma_N + im_N)e^{-\sigma_N z}e^{im_N z} - B^-(\sigma_N + im_N)e^{-\sigma_N z}e^{-im_N z}. \quad (4.39)$$

Unlike at the bottom of the domain, the streamfunction values are known and the amplitudes remain to be found. Defining $\delta \equiv \cos(m_N z_N)e^{\sigma_N z_N}/2m_N$

and $\gamma \equiv \sin(m_N z_N)\, e^{\sigma_N z_N}/2m_N$, wave amplitudes B^+ and B^- are found from calculated streamfunction values at the top of the domain:

$$\begin{bmatrix} \mathrm{Re}\{B^+\} \\ \mathrm{Im}\{B^+\} \\ \mathrm{Re}\{B^-\} \\ \mathrm{Im}\{B^-\} \end{bmatrix} = \begin{bmatrix} m_N\delta - \sigma_N\gamma & \sigma_N\delta + m_N\gamma & -\gamma & \delta \\ -\sigma_N\delta - m_N\gamma & m_N\delta - \sigma_N\gamma & -\delta & -\gamma \\ m_N\delta - \sigma_N\gamma & -\sigma_N\delta - m_N\gamma & -\gamma & -\delta \\ \sigma_N\delta + m_N\gamma & m_N\delta - \sigma_N\gamma & \delta & -\gamma \end{bmatrix} \begin{bmatrix} \mathrm{Re}\{\phi_N\} \\ \mathrm{Im}\{\phi_N\} \\ \mathrm{Re}\{\phi'_N\} \\ \mathrm{Im}\{\phi'_N\} \end{bmatrix}. \tag{4.40}$$

Given incident and reflected wave amplitudes, the outgoing and returning wave amplitudes may be found. As such, the initial condition driver discussed in section 2.3.2 may be applied to find the appropriate choice of A^+ and A^- that, upon integration, $B^- = 0$. With the initial conditions properly selected and the streamfunction amplitudes known, the strength of the wave reflection, R, is then calculated as in equation (2.34).

Chapter 5

Anelastic Simulations

5.1 Introduction

Using the numerical techniques developed in the previous chapter, a computer code is developed to model anelastic internal gravity waves. This code is applied to the piecewise-linear shear profiles considered by Brown and Sutherland (2007). In the limit of large density scale height, H_ρ, the numerical results are compared to their analytic results as a test. The density scale height is then reduced, allowing the anelastic effects to dominate. In section 5.3 the propagation of internal waves generated over Jan Mayen island in the lee of Mount Beerenberg is considered. Atmospheric background profiles observed near the region when internal waves were present are input into the code and resulting transmission characteristics found.

5.2 Piecewise-linear Shear

The analytic results of Brown and Sutherland (2007), which apply in the limit as density scale height becomes large, are presented in section 5.2.1. The effects of finite density scale height are considered in section 5.2.2 and the transmission characteristics are found using the numerical code outlined in

chapter 4.

5.2.1 Analytic Results

Brown and Sutherland (2007) consider the propagation of internal waves through a uniformly increasing shear coincident with a buoyancy frequency gap. Their study was restricted to small-amplitude two-dimensional disturbances in a non-rotating, inviscid, Boussinesq fluid. Explicitly, the background shear and squared buoyancy frequency profiles they considered are

$$\bar{U}(z) = \begin{cases} 0 & \text{for } z \leq L \\ \frac{U_0}{L}(z - L) & \text{for } L \leq z \leq 2L \\ U_0 & \text{for } z \geq 2L \end{cases} \tag{5.1}$$

and

$$N(z) = \begin{cases} N_0^2 & \text{for } z < L \\ 0 & \text{for } L \leq z \leq 2L\,, \\ N_0^2 & \text{for } z > 2L \end{cases} \tag{5.2}$$

respectively. The shear profile is plotted schematically in Figure 5.1*a* and the squared buoyancy frequency profile is shown in Figure 5.1*b*.

In characterizing the background profiles described by equations (5.1) and (5.2), the strength of the maximum shear relative to the maximum buoyancy frequency is relevant. This parameter is described by the bulk Richardson number as defined in equation (3.5). For large bulk Richardson number the shear is weak. In the limit as it approaches infinity the background is stationary. When $\mathrm{Ri_b} \approx 1$ the shear is strong relative to the buoyancy frequency and significantly affects the propagation of internal waves.

Using these profiles, in each of the three regions $z < L$, $L \leq z \leq 2L$ and $z > 2L$ the coefficients to the Taylor-Goldstein equation (2.12) are constant. As such, streamfunction solutions may be found in each region as discussed in section 2.3.2. Using appropriate matching conditions at the boundaries

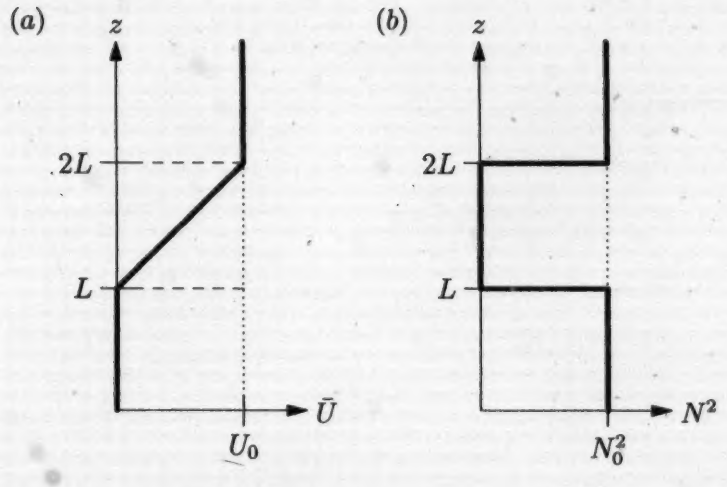

Figure 5.1: (*a*) Background horizontal shear and (*b*) Boussinesq buoyancy frequency profiles.

between the three regions, Brown and Sutherland (2007) were able to find the streamfunction amplitude everywhere in the domain and thus characterize the internal wave transmission. Using the explicit transmission formula found in their paper, the transmission characteristic is plotted for $\mathrm{Ri_b} = 100,\ 10$, and 1 in the first row of Figure 5.3. In this plot, the incident wave frequency has been nondimensionalized by the background buoyancy frequency at $z = 0$ as

$$\hat{\omega} = \frac{\omega}{N_0} \tag{5.3}$$

and the horizontal wavenumber nondimensionalized by the gap width

$$\hat{k} = kL. \tag{5.4}$$

Comparison of the density scale height, H_ρ, at ground level to the domain length, $3L$, provides a measure of the anelastic effects. For $H_\rho/L \approx 1$ the density scale height is large relative to the gap width and anelastic effects dominate, when H_ρ/L is large the flow is more Boussinesq. As discussed

in section 4.2, the Boussinesq approximation is equivalent to the anelastic approximation in the limit as density scale height approaches infinity. As such, the analytic Boussinesq results are presented in Figure 5.3 as anelastic results in the limit as $H_\rho/L = \infty$.

5.2.2 Numerical Results

Using the numerical techniques outlined in chapter 4, the results of Brown and Sutherland (2007) are extended to consider the effects of finite density scale height upon tunnelling. As the equations are now fully anelastic, the buoyancy frequency profiles are found in terms of prescribed potential temperature profile

$$\bar{\theta}(z) = \begin{cases} \theta_0 \exp\left(\frac{z}{H_\theta}\right) & \text{for } z \leq L \\ \theta_0 \exp\left(\frac{L}{H_\theta}\right) & \text{for } L \leq z \leq 2L\,, \\ \theta_0 \exp\left(\frac{z-L}{H_\theta}\right) & \text{for } z \geq 2L \end{cases} \tag{5.5}$$

as plotted schematically in Figure 5.2*a*. The potential temperature-based scale height,

$$H_\theta = \frac{g}{N^2_{\theta_0}}, \tag{5.6}$$

is the length scale over which the background potential temperature changes by a factor of e.

Applying equation (1.4) to the potential temperature profile given above, the resulting potential temperature defined squared buoyancy frequency is

$$N^2_\theta(z) = \begin{cases} N^2_{\theta_0} & \text{for } z < L \\ 0 & \text{for } L \leq z \leq 2L\,, \\ N^2_{\theta_0} & \text{for } z > 2L \end{cases} \tag{5.7}$$

as plotted in Figure 5.2*b*. Applying equation (B.8) to the potential temperature

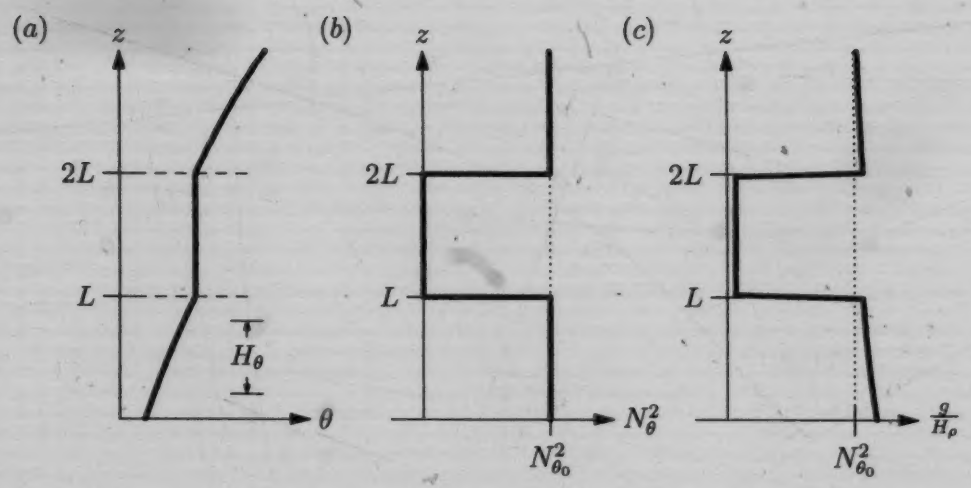

Figure 5.2: (a) Background potential temperature, (b) potential temperature defined squared buoyancy frequency and (c) density scale height profiles. Density scale height profile is presented for $H_\rho/L = 1$ case.

profiles, the density scale height profile is found

$$gH_\rho^{-1}(z) = \begin{cases} N_{\theta_0}^2 + \frac{g}{\kappa}\left[\left(\frac{\theta_0}{\Gamma} - H_\theta\right)e^{\left(\frac{z}{H_\theta}\right)} + H_\theta\right]^{-1} & \text{for } z < L \\ \frac{g}{\kappa}\left[\left(\frac{\theta_0}{\Gamma} - H_\theta\right)e^{\left(\frac{L}{H_\theta}\right)} + H_\theta + L - z\right]^{-1} & \text{for } L \le z \le 2L \\ N_{\theta_0}^2 + \frac{g}{\kappa}\left[\left(\frac{\theta_0}{\Gamma} - H_\theta\right)e^{\left(\frac{z-L}{H_\theta}\right)}\right. & \\ \qquad \left. - H_\theta + (2H_\theta - L)\,e^{\left(\frac{z-2L}{H_\theta}\right)}\right]^{-1} & \text{for } z > 2L \end{cases} \tag{5.8}$$

In the limit as H_θ becomes large, this reduces to

$$gH_\rho^{-1}(z) = \begin{cases} N_{\theta_0}^2 + \frac{g}{\kappa}\left[\frac{\theta_0}{\Gamma}\right]^{-1} & \text{for } z < L \\ \frac{g}{\kappa}\left[\left(\frac{\theta_0}{\Gamma} + L - z\right)\right]^{-1} & \text{for } L \le z \le 2L\,, \\ N_{\theta_0}^2 + \frac{g}{\kappa}\left[\frac{\theta_0}{\Gamma} - L\right]^{-1} & \text{for } z > 2L \end{cases} \tag{5.9}$$

For typical atmospheric profiles $\Gamma L \ll \theta_0$ and $\frac{\Gamma g}{\theta_0 \kappa} \ll N_\theta^2$ so that

$$gH_\rho^{-1}(z) \approx \begin{cases} N_{\theta_0}^2 & \text{for } z < L \\ 0 & \text{for } L \le z \le 2L \\ N_{\theta_0}^2 & \text{for } z > 2L \end{cases} \tag{5.10}$$

when H_θ is large and the anelastic buoyancy frequency profiles reduce to the equivalent Boussinesq profiles considered by Brown and Sutherland (2007). Furthermore, the background shear profiles used in the numerical simulations are those prescribed by equation (5.1), so the problem considered here is the anelastic extension of their Boussinesq result.

Using the profiles prescribed by equations (5.5) and (5.1) as input to the anelastic code, transmission characteristics are found for $\mathrm{Ri_b} = 100,\ 10$, and 1 when ground-level $H_\rho/L = 100,\ 10$, and 1. The transmission characteristics are plotted in Figure 5.3. In each of the plots in the figure the superimposed broken white lines delineate significant boundaries in $\hat{\omega} - \hat{k}$ space. The dashed lines mark the boundary between regions where solutions are wavelike at both the top and bottom of the domain and where they are not wavelike for the equivalent Boussinesq system. The dashed-dotted lines mark the boundary between regions where waves encounter a critical layer somewhere in the flow and where critical layers are not encountered.

The Frobenius solver is used in the region to the right of the dashed-dotted line. Here specific frequency and wavenumber combinations may result in numerical errors that prevent calculation of transmission coefficient. These errors are a consequence of the cut-off condition used to invoke the Frobenius solver. If the region over which the Frobenius solver is required is too large then the code may not be able to accurately determine polynomial fits for the anelastic Taylor-Goldstein equation, in which case transmission cannot be calculated. In Figure 5.3 a filter is applied to suppress this spurious data. At points where the transmission coefficient cannot be computed it is taken as the average of the value at the four nearest gridpoints.

In the left column of Figure 5.3 transmission is considered for $\mathrm{Ri_b} = 100$.

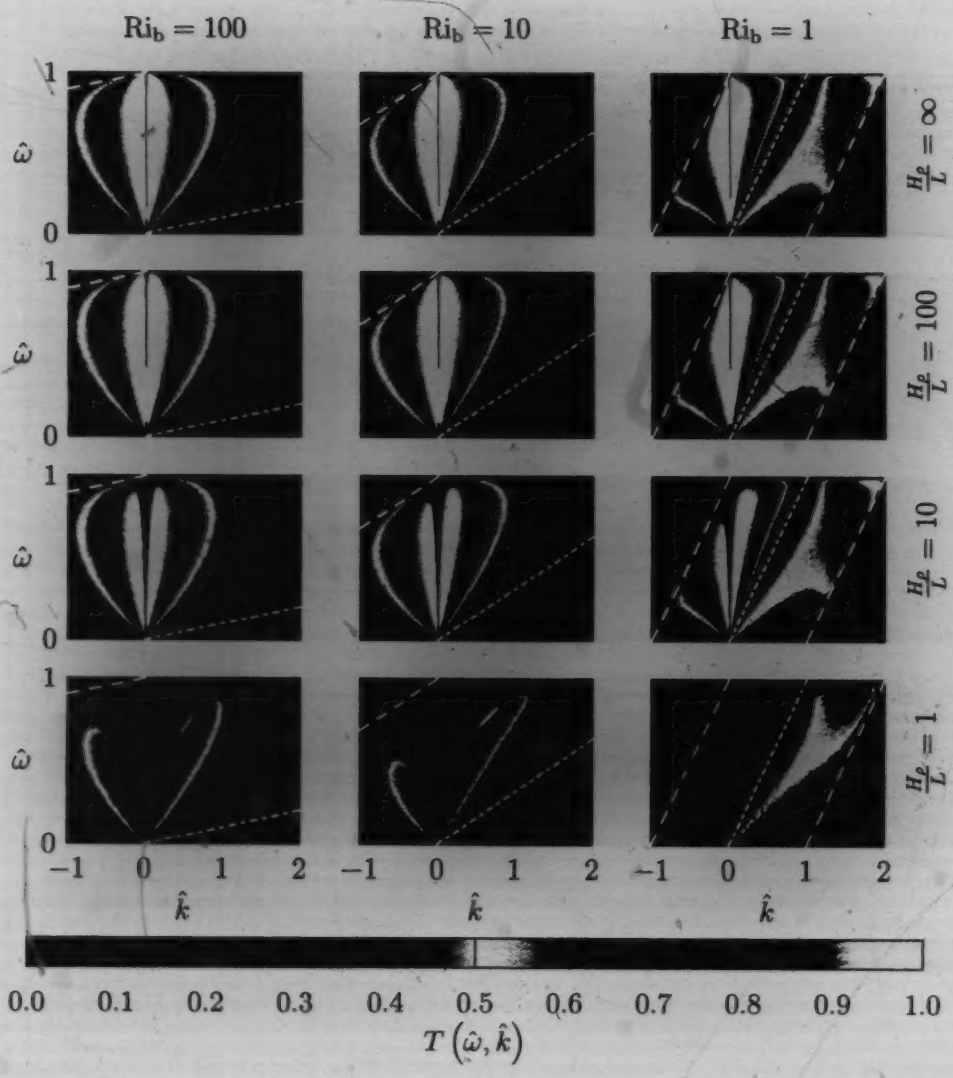

Figure 5.3: Transmission is plotted as a function of nondimensional incident wave frequency and horizontal wavenumber calculated for piecewise-linear shear profiles. Bulk Richardson number is constant over vertical columns and relative scale height H_ρ/L constant over horizontal rows. $H_\rho/L = \infty$ plots are computed from analytic formula found by Brown and Sutherland (2007), finite H_ρ/L plots are computed using the numerical solver.

For large bulk Richardson number, the shear flow is less significant than the buoyancy frequency in determining the internal wave propagation. As expected, the transmission characteristics in the upper-left panel, which corresponds to the Boussinesq approximation, is nearly identical to that found by Sutherland and Yewchuk (2004) who considered similar profiles with $U_0 = 0$.

Moving down the $\mathrm{Ri_b} = 100$ column in the figure, the potential temperature scale height is reduced relative to the gap width thus making anelastic effects more significant. The $H_\rho/L = 100$ row is presented essentially as a diagnostic test on the solver. As the density scale height is two orders of magnitude larger than the gap width the anelastic effects are not significant. As such, the transmission characteristics are nearly identical to those of the Boussinesq case, demonstrating the efficacy of the code. For $H_\rho/L = 10$ the anelastic effects begin to become significant. Examining the third panel from the top on the left, it is clear that the region about $\hat{k} = 0$ where wave transmission cannot be calculated is expanding. Transmission calculation is not possible in this region because the solutions to the anelastic Taylor-Goldstein equation are not wavelike. A discussion of why solutions are wavelike over a smaller region of $\hat{\omega} - \hat{k}$ space is presented in section 4.3.2 (see equation (4.34)). This effect is even more predominant for $H_\rho/L = 1$ as the flow becomes highly anelastic. As the central region where transmission cannot be computed grows, the transmission limit is moved outwards in $\hat{k}$-space. Examining the bottom left plot in the figure, it is clear that transmission is greater for larger horizontal wavenumber than in cases with larger density scale height. Aside from this shift, the transmission plots share similar characteristics. For each plot there is strong transmission in a central region that decreases as the wavenumber magnitude increases and peaks near $\hat{\omega} = 0.7$. This behaviour is reproduced as

the bulk Richardson number decreases.

In the middle column of the figure shear strength is increased so that $\mathrm{Ri_b} = 10$. In the region of the plots left of the dashed-dotted line, where a critical layer is not encountered anywhere in the flow, the increased shear acts to deform but not significantly alter the transmission characteristics. There is still strong transmission for small $\hat{k}$ but the transition to relatively low transmission occurs over a shorter range relative to the $\mathrm{Ri_b} = 100$ case. In the region to the right of the dashed-dotted line a critical layer is encountered somewhere in the flow. As in the $\mathrm{Ri_b} = 100$ case transmission is very low throughout this region of the plot, however it has increased slightly. For smaller density scale height, the central region where transmission cannot be computed is wider: the transmission characteristics expand outwards in $\hat{k}$-space. At the boundaries of this region transmission is found to be larger for greater horizontal wavenumbers.

In the rightmost column of the figure transmission characteristics are plotted for $\mathrm{Ri_b} = 1$. In this case the effects of the horizontal flow are clearly manifest. In the region of the plot to the left of the dashed-dotted line, where waves do not encounter critical layers, the transmission characteristics are further restricted to a smaller range of $\hat{k}$ and $\hat{\omega}$, but still maintain properties similar to the lower shear cases. Transmission is high near $\hat{k} = 0$ and gradually decreases as the magnitude of the horizontal wavenumber becomes larger. Significant differences from the lower shear cases appear in the region to the right of the dashed-dotted line, where waves encounter a critical layer somewhere in the flow. Near perfect transmission is now possible when a critical layer is encountered for extreme values of frequency and wavenumber in the Boussinesq limit. This result is reproduced in both the $H_\rho/L = 100$ and

$H_\rho/L = 10$ cases. However, for $H_\rho/L = 1$ the reduced range of frequency and wavenumber over which transmission is possible becomes significant. The region over which transmission is possible in the non-critical regime is very small and the transmission peak values are only about 0.5. In the region where a critical layer is encountered maximum transmission of about 0.7 is possible. For large $\hat{k}$ and $\hat{\omega}$, where transmission was nearly unity in the greater density scale height cases, transmission is not possible due to non-wavelike solutions.

Anelastic effects have reduced the transmission coefficient over the domain. In each case considered here, reducing scale height introduced a central region where wave transmission was not possible. As this central region grew the transmission characteristics expanded outward in $\hat{k}$-space so that transmission was larger for greater horizontal wavenumbers. The outward expansion of the transmission characteristics was less significant than the expansion of the region where transmission could not be computed, in that the overall effect of reducing scale height is to decrease transmission throughout the domain.

5.3 Jan Mayen

Atmospheric internal waves are generated principally through two different phenomena: storms cause disturbances that launch internal waves into the stratosphere, and surface flow over rough topography generates internal waves that propagate upwards in the troposphere. Eckermann et al. (2006) model the propagation of topographically generated internal waves over Jan Mayen island (71°N, 8.4°W). Jan Mayen is an ideal candidate for internal wave generation studies due to its relative isolation in the North Atlantic Ocean and its significant surface elevation. Mount Beerenberg, with peak elevation of approximately 2.3 km and diameter 15 km, dominates the island topography.

Previous studies by Gjevik and Marthinsen (1978) and Simard and Peltier (1982) associate cloud banding near Jan Mayen with trapped lee waves generated by flow over Mount Beerenberg.

5.3.1 Background

Using background buoyancy frequency and shear profiles gathered from radiosonde data collected at 1200 UTC on 25 January 2000, a period when wave-like cloud banding was observed downstream of the island by satellite imagery, Eckermann et al. (2006) attempt to 'hindcast' observed wave patterns using a three-dimensional Fourier-ray model. The observed buoyancy frequency and shear data used are plotted in Figure 5.4. Although the recorded wind data is available as both a north- and east-ward horizontal component, in the figure these components are added in quadrature to determine horizontal velocity magnitude. The direction of the flow is height dependent but deviates little from approximately 36° north of east throughout the domain. The horizontal shear magnitude is considered so that a two-dimensional approximation may be invoked. The relatively low resolution (one sample per 500 m of vertical traverse) profiles are upsampled to much higher resolution as is required for the Fourier-ray solver.

Through analysis of Scorer parameters (a measure of vertical trapping of linear waves) found from these physical profiles, Eckermann et al. (2006) developed heuristic arguments for wave reflection downstream of Mount Beerenberg. Using atmospheric data gathered from two different sources and applying three different definitions of Scorer parameter they determined that, for a typical horizontal wavelength of 30 km there was a 'reflection level' somewhere between 5 and 8 km altitude. Furthermore, due to a stable surface boundary

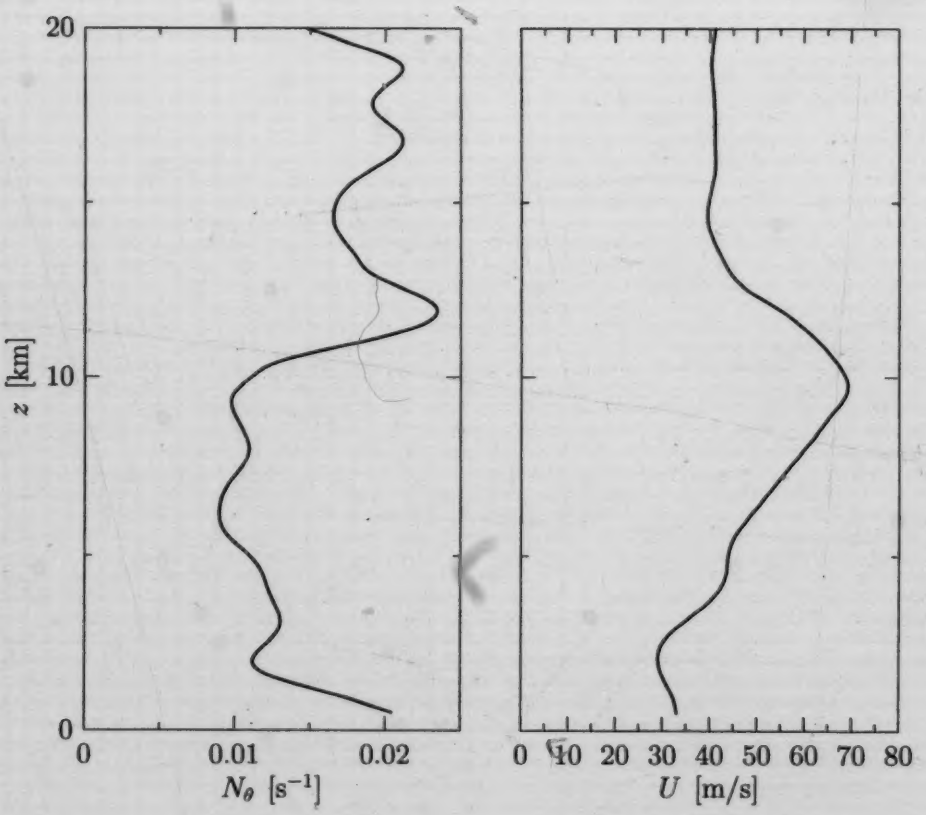

Figure 5.4: Buoyancy frequency and mean horizontal wind observed over Jan Mayen at 1200 UTC on 25 January 2000. [Adapted from Eckermann et al. (2006)]

layer and strong surface flow, waves incident upon the surface would not be absorbed and instead reflect back upwards. As such, they concluded that the prevailing atmospheric conditions gave rise to a waveguide that would vertically trap internal waves allowing them to propagate well downstream of their generation point.

Eckermann et al. (2006) apply their ad hoc three-dimensional Fourier-ray method to model non-hydrostatic mountain-wave fields over Jan Mayen. In Figure 5.5*a*, a reproduction of their Figure 9, a vertical cross section of the vertical velocity field, taken along a path coincident with the wind, is presented. In this plot a large amplitude wave, with vertical velocities of approximately 4 m/s and horizontal wavelength $k = 0.14$ km^{-1}, is trapped in a horizontal waveguide with bottom near ground level and top at approximately 10 km, coincident with the peak in background horizontal flow. Vertical velocities remain large and have horizontal periodicity as far as 200 km beyond the point of generation in the waveguide. Above the waveguide there is comparatively little wave induced vertical flow. Furthermore, the wave amplitude decreases significantly along the horizontal domain – about 150 km downstream of Mount Beerenberg the vertical flow has nearly dissipated.

When they performed the same simulations using a considerably more computationally expensive nonlinear numerical model significantly different vertical velocity profiles were observed. Examining Figure 5.5*b*, it is clear that the downstream vertical velocity does not remain large well beyond the generation point and there is significant wave energy in the stratosphere. It is apparent that wave energy 'trapped' in the waveguide can escape through the evanescent region upwards in the vertical domain. In fact, Eckermann et al. (2006) go so far as to suggest that the 'leakiness' of the waveguide is

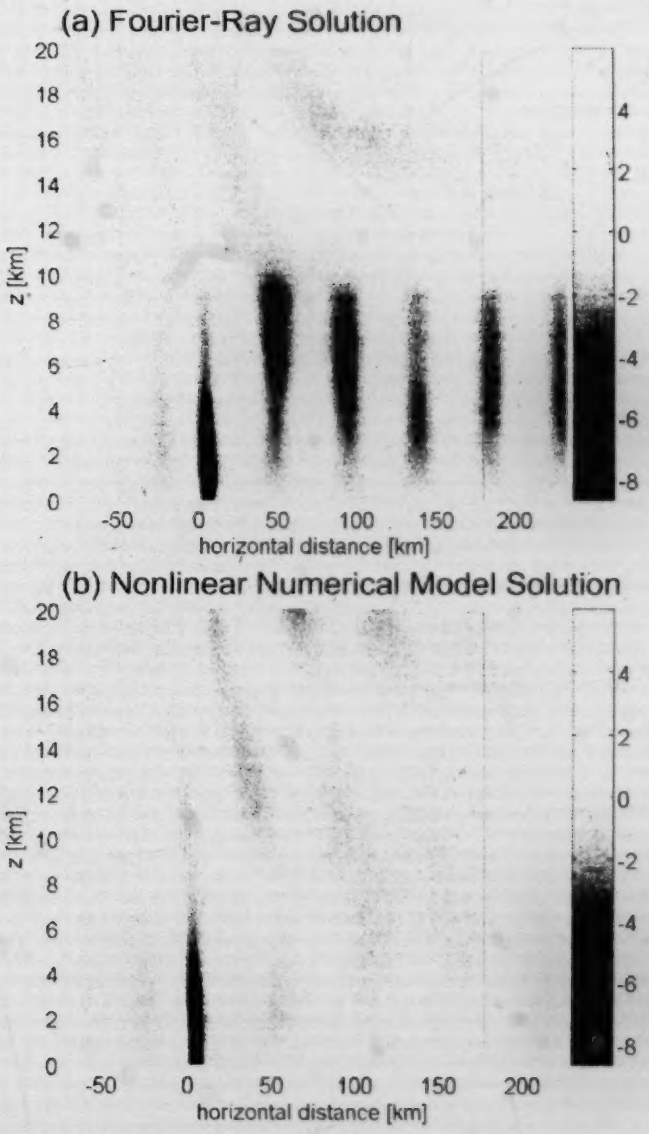

Figure 5.5: "Vertical cross sections of vertical velocity in m s^{-1} (see grayscale bars) at t = 4 h along the line indicated in Fig. 8. (a) Fourier-ray solution. Minimum value is -7.8 m s^{-1} and maximum value is -6.1 m s^{-1}. (b) Nonlinear numerical model solution. Minimum value is -8.7 m s^{-1} and maximum value is -5.8 m s^{-1}." [Adapted from Figure 9 from Eckermann et al. (2006). Reproduced with permission from the American Meteorological Society.]

due to tunnelling of the internal waves through an evanescent region near the tropopause into the stratosphere. This tunnelling is a physical phenomenon that their Fourier-ray model cannot reproduce. The techniques we developed in chapter 4 can be applied to such a tunnelling problem without significantly increasing computation time.

5.3.2 Numerical Results

The Jan Mayen background profiles, as plotted in Figure 5.4, are input into the anelastic numerical solver and the resulting transmission characteristics are found. The transmission coefficient is plotted for the entire range of incident fréquency and horizontal wavenumber over which wavelike solutions exist at the bottom and top of the domain in Figure 5.6.

As in previous transmission characteristic plots, regions plotted in black correspond to regions in which transmission could not be computed. In the the areas on the far left and right sides of the plot, frequency and horizontal wavenumber combinations are such that solutions to the anelastic Taylor-Goldstein equation are not wavelike at either the bottom or top of the domain, so propagating wave solutions are not possible. The lower of the two dashed-dotted white lines corresponds to incident frequency and wavenumber combinations with resulting wave velocity equal to the minimum background horizontal flow speed. Likewise, the upper white line denotes frequency and wavenumber combinations with wave speeds equal to the maximum horizontal flow velocity. As the horizontal flow speed is continuous, in the region between these two lines the incident wave speed matches that of the background flow somewhere in the vertical domain. For frequency and wavenumber combinations outside this region the waves do not encounter a critical layer anywhere

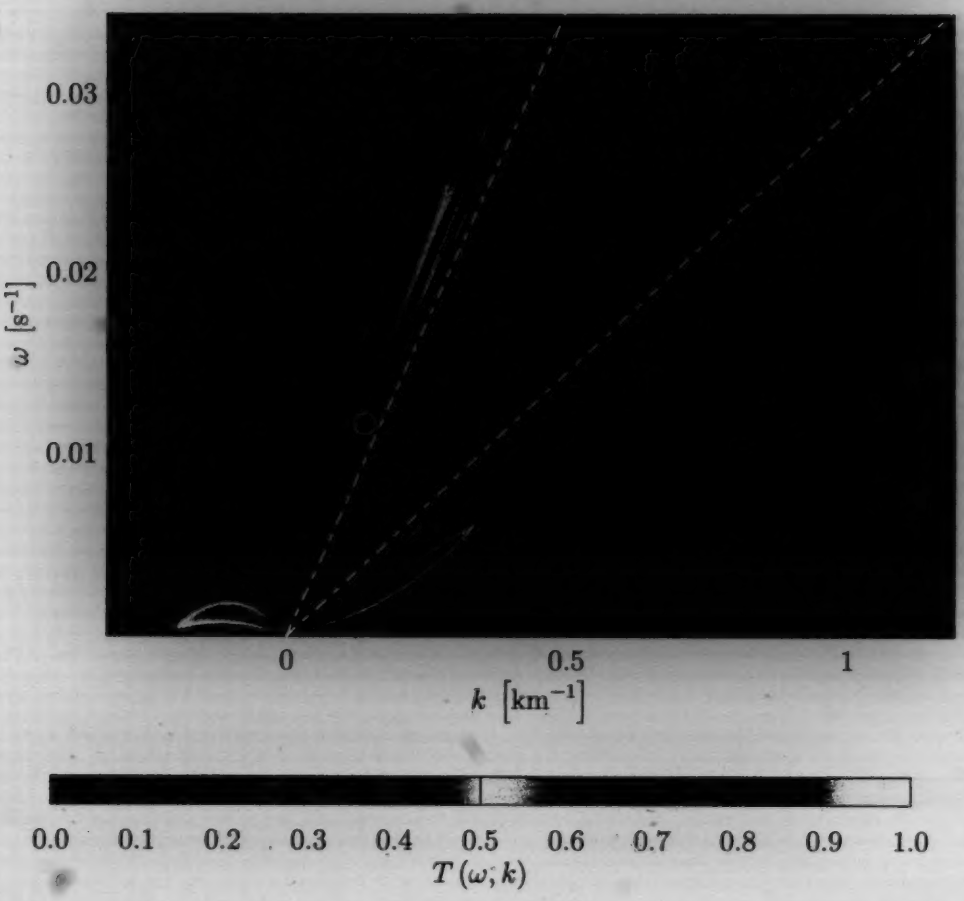

Figure 5.6: Transmission as a function of incident wave frequency and wavenumber for atmospheric conditions observed over Jan Mayen (as plotted in Figure 5.4). White circle highlights frequency, as predicted by Aguilar and Sutherland (2006), and horizontal wavenumber of trapped waves in Figure 5.5*a*.

in the vertical domain, for parameters inside this region the waves encounter at least one critical layer. As the atmospheric profiles are very stable, any atmospheric instability would overturn quickly and evolve into a stable state, the gradient Richardson number is larger than 1/4 everywhere in the flow. As such, transmission calculation is not possible when a critical layer is present.

In the region to the right of the dashed-dotted line in Figure 5.6, where waves move slower than the minimum horizontal flow in the background profiles, transmission is relatively weak. At lower frequencies there are three bands of higher transmission due to a resonance between waves and vertical profiles that results in greater transmission, as discussed in Sutherland and Yewchuk (2004). For forward propagating waves moving more quickly than the maximum horizontal flow speed, transmission is relatively high over nearly the entire region. Transmission decreases at larger frequencies but remains larger than 0.5 for nearly all wavenumbers in the region when $\omega < 1.3$. Again there are bands of stronger transmission suggesting resonant interactions with the profiles. For negative horizontal wavenumbers, which may be interpreted physically as downward travelling waves, transmission is weak outside of a narrow band of relatively large transmission. Only relatively low frequency waves are possible in this regime.

To apply the numerical solver to waves observed over Mount Beerenberg the temporal frequency of wave generation is estimated. In characterizing wave generation by flow over topography it is useful to define the Froude number

$$\mathrm{Fr} = \frac{2\pi U_0}{N_0 L}, \tag{5.11}$$

where U_0 and N_0 are the flow speed and buoyancy frequency near the point of generation, respectively, and L is the horizontal scale of of the topography. For the flow over mount Beerenberg considered here $\mathrm{Fr} \approx 1$.

Aguilar and Sutherland (2006) performed laboratory experiments examining the generation of internal waves by stratified flow over topography. They found that lee waves generated by flows with Froude number near unity had $\omega \approx 0.72N_0$. As such, for the atmospheric profiles observed over Jan Mayen, lee waves will have frequency $\omega \approx 0.012$ s^{-1}. From the vertical velocity field plotted in Figure 5.5*a*, it is clear that in the solution produced by the Fourier-ray solver a large amplitude wave with horizontal wavelength $k = 0.14$ km^{-1} is trapped in the troposphere. Using these parameters the streamfunction is calculated numerically for the Jan Mayen atmospheric profiles, the transmission coefficient is 0.69. The resulting streamfunction magnitude and phase are plotted in Figure 5.7.

In a region beginning at altitude 9.26 km and ending at $z = 10.12$ km the coefficients of the anelastic Taylor-Goldstein equations are such that the waves become evanescent. In the evanescent region the streamfunction phase decreases sharply and the streamfunction magnitude halves. Beyond the evanescent region wavelike propagation is again possible and the streamfunction magnitude does not fall any further. This suggests that, contrary to the Fourier-ray results of Eckermann et al. (2006), significant amounts of wave energy can penetrate through the tropopause into the stratosphere.

Using the transmission coefficient calculated for trapped waves simulated by Eckermann et al. (2006) an estimate for how much wave energy escapes the duct as the wave propagates horizontally is found. Transmission coefficient is a measure of energy flux for periodic, monochromatic plane waves. Trapped waves are essentially periodic waves that propagate to the top of their waveguide and then reflect back to the bottom of the waveguide where they are again reflected back upwards. As such, the transmission coefficient

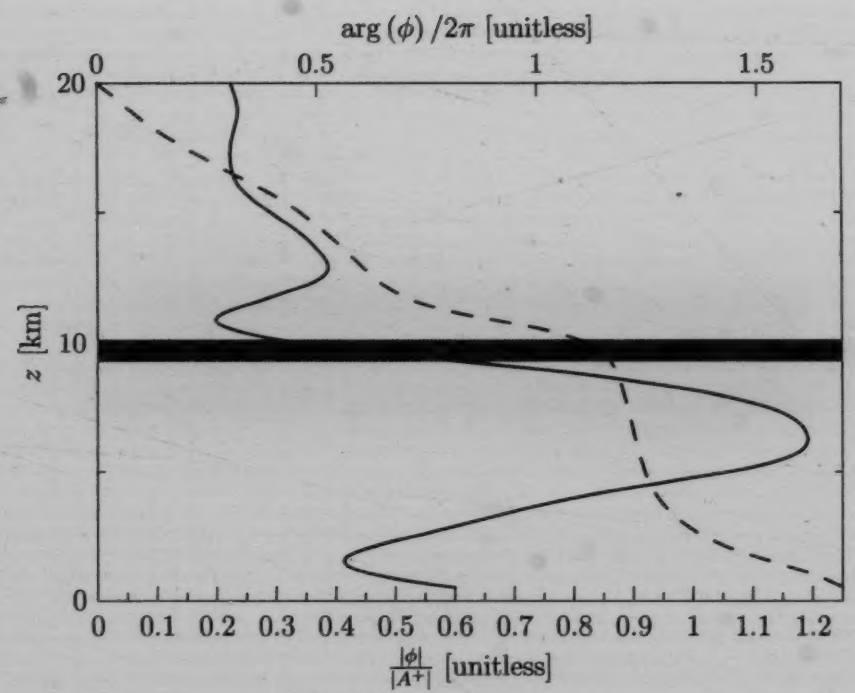

Figure 5.7: Streamfunction magnitude (solid line) and phase (dashed line) calculated for waves with horizontal wavenumber $k = 0.14$ km^{-1} and frequency $\omega = 0.012$ s^{-1} using Jan Mayen background profiles presented in Figure 5.4. A region near $z = 10$ km where the waves are evanescent is highlighted.

is a measure of how much energy, E, escapes the waveguide each horizontal wavelength, $\lambda = 2\pi/k$,

$$\frac{1}{E}\frac{\partial E}{\partial x} = -\frac{T}{\lambda}, \tag{5.12}$$

so that energy remaining in the waveguide decays as

$$E(x) \propto e^{-Tx/\lambda}. \tag{5.13}$$

Over the length of the horizontal domain considered in the Fourier-ray solutions the trapped wave traverses approximately five horizontal wavelengths. Using the computed transmission coefficient, approximately 0.2% of the wave energy will remain in the waveguide at the far right bound of the domain. As energy is related to the square of velocity, it is expected that vertical velocities near the end of the domain are approximately 5% of those at the beginning of the waveguide. These results are consistent with the nonlinear numerical results plotted in Figure 5.5*b*.

Chapter 6

Summary and Conclusions

We developed numerical techniques to model the propagation of small-amplitude two-dimensional internal gravity waves through non-rotating inviscid fluids in the Boussinesq and anelastic approximations. Using these techniques, computer codes were written to compute transmission coefficients for internal gravity wave transmission given arbitrary background horizontal flow and buoyancy frequency profiles and specified wave frequencies and horizontal wavenumbers.

In the Boussinesq approximation, which applies when the density changes little over the vertical extent of the domain, internal wave propagation is described by the Taylor-Goldstein equation. Numerical integration is possible when the wave speed is not that of the background flow anywhere in the domain. If the wave speed does match that of the background horizontal flow, then a critical layer is encountered. Integration across a critical layer is possible using the method of Frobenius, however it may only be applied if the local gradient Richardson is less than 1/4. If $Ri_g > 1/4$ waves develop rapid oscillations near the singularity, leading to efficient wave dissipation.

The Boussinesq numerical solver was applied to three sets of background profiles. First, transmission across an unsheared weakly stratified fluid was

considered. We found that WKB theory accurately predicts, within 98%, near perfect transmission if the vertical wavelength is smaller than the buoyancy frequency transition length. For longer wavelengths, the calculated transmission was lower than the WKB prediction. Transmission across a uniformly stratified unstable shear layer was then considered, and the effects of decreasing the strength of the stratification relative to the shear examined. It was found that wave transmission is strong in the absence of a critical layer, and typically increases with shear strength. If a critical layer is present, then the transmission increases with increasing shear, but the range of frequency and wavenumber combinations for which $Ri_g < 1/4$ decreases. The third application of the Boussinesq numerical solver was to a mixed shear layer developed by allowing the previously considered shear layers to go unstable and evolve into a quasi-steady state. Despite the introduction of a well mixed layer with low buoyancy frequency, the quantitative behaviour were similar to those found for the unstable shear layer.

Using Navier-Stokes equations in the anelastic approximation, an anelastic extension of the Taylor-Goldstein equation was found. The governing equation remains a second order ordinary differential equation however, in contrast to the Boussinesq equation, the coefficient of the first order term is non-zero. This introduces new dynamics in the wave propagation; in addition to oscillation, the streamfunction solutions in regions of constant background profiles now decay exponentially. Although the streamfunction amplitudes decay the wave induced velocities typically increase significantly with altitude. In defining mass flux streamfunction the streamfunction amplitudes are divided by local density to determine velocity. For atmospheric waves the density decrease, which acts to increase wave velocities, is much stronger than the streamfunc-

tion amplitude decrease, which acts to reduce displacement velocity. As such, the wave-induced flow velocities grow at exponential rates with increasing altitude. This exponential growth is required to conserve momentum: as upward propagating disturbances encounter less dense fluid amplitude must increase. Furthermore, as wavelike solutions are required at the top and bottom of the domain for transmission calculation, the range of frequency and horizontal wavenumber over which transmission is possible decreases relative to the equivalent Boussinesq system.

The anelastic solver was applied to two sets of background profiles. The piecewise-linear shear profiles of Brown and Sutherland (2007) are considered and equivalent anelastic profiles developed. The anelastic numerical solver is applied to a series of profiles with decreasing density scale height, thus increasing the anelastic effects. Profiles with large density scale height were first considered and the analytic results of Brown and Sutherland (2007) are reproduced. As density scale height decreases the region of the transmission characteristics where solutions are not wavelike grows. However, the transmission plots maintain similar characteristics independent of density scale height.

The anelastic solver was then applied to physical profiles observed over Jan Mayen island during a period where mountain generated internal waves were observed in the region. In a previous study by Eckermann et al. (2006) Fourier-ray tracing methods where used to model internal wave propagation over Jan Mayen. They found that waves were trapped in a horizontal waveguide between the ground and tropopause and could not propagate into the stratosphere. However, upon application of our anelastic numerical model we found that waves could tunnel through an evanescent region coincident with the tropopause and thus radiate wave energy into the stratosphere. This con-

clusion is supported by both satellite observations of the wave event and fully nonlinear numerical simulations conducted by Eckermann et al. (2006).

In future work it may be useful to implement our numerical techniques into weather models to better simulate internal wave propagation. Specifically, there are many models that use Fourier-ray methods to calculate wave propagation. As demonstrated in chapter 5 these ray tracing techniques are not effective when there are regions in the flow where wave solutions become evanescent. In the atmosphere, the poorly stratified mesosphere is flanked by the strongly stratified thermosphere and stratosphere. Using our methods transmission may be found for waves that propagate from the stratosphere through the mesosphere, where they become evanescent, into the thermosphere. Similarly, in the ocean, our techniques may be applied to model internal waves as they propagate from the main to seasonal thermocline, passing through a region where they are evanescent. In both these problems internal waves transport energy away from the surface. As such, accurate measure of how much energy is transported is very important in weather modelling.

Bibliography

Aguilar, D. A. and B. R. Sutherland (2006). Internal wave generation from rough topography. *Phys. Fluids 18*, Art. No. 066603.

Alexander, M. J., P. May, and J. Beres (2004). Gravity waves generated by convection in the Darwin Area Wave Experiment. *J. Geophys. Res. 109*(D20S04). doi:10.1029/2004JD004729.

Andrews, D. G. and M. E. McIntyre (1978). On wave action and its relatives. *J. Fluid Mech. 89*, 647–664.

Batchelor, G. K. (1953). The conditions for dynamical similarity of motions of a frictionless perfect-gas atmosphere. *Quart. J. Roy. Meteor. Soc. 79*, 224–235.

Boyce, W. E. and R. C. DiPrima (2005). *Elementary Differential Equations and Boundary Value Problems* (8th ed.). New York: John Wiley and Sons.

Broutman, D., J. W. Rottman, and S. D. Eckermann (2004). Ray methods for internal waves in the atmosphere and ocean. *Annu. Rev. Fluid Mech. 36*, 233–253.

Brown, G. L. and B. R. Sutherland (2007). Internal wave tunnelling through non-uniformly stratified shear flow. *Atmos. Ocean 45*, 47–56.

Dillon, T. M., J. N. Moum, T. K. Chereskin, and D. R. Caldwell (1989). Zonal momentum balance at the equator. *J. Phys. Oceanogr. 19*, 561–570.

Drazin, P. G. and W. H. Reid (1981). *Hydrodynamic Stability.* Cambridge, England: Cambridge University Press.

Duin, C. A. V. and H. Kelder (1981). Reflection properties of internal gravity waves incident upon a hyperbolic tangent shear layer. *J. Fluid Mech. 120*, 505–521.

Eckart, C. (1961). Internal waves in the ocean. *Phys. Fluids 4*, 791–799.

Eckermann, S. D., D. Broutman, J. Ma, and J. Lindeman (2006). Fourier-ray modeling of short-wavelength trapped lee waves observed in infrared satellite imagery near Jan Mayen. *Mon. Wea. Rev. 134*, 2830–2848.

Eckermann, S. D., A. Dornbrack, S. B. Vosper, H. Flentje, M. J. Mahoney, T. P. Bui, and K. S. Carslaw (2006). Mountain wave-induced polar stratospheric cloud forecasts for aircraft science flights during SOLVE/THESEO 2000. *Wea. Forecasting 21*, 42–68.

Eliassen, A. and E. Palm (1961). On the transfer of energy in stationary mountain waves. *Geofys. Publ. 22*, 1–23.

Eltayeb, I. A. and J. F. McKenzie (1975). Critical-level behaviour and wave amplification of a gravity wave incident upon a shear layer. *J. Fluid Mech. 72*, 661–671.

Firing, E. (1987). Deep zonal currents in the central equatorial Pacific. *J. Mar. Res. 45*, 791–812.

Fritts, D. C. and L. Yuan (1989). An analysis of gravity wave ducting in the atmosphere: Eckart's resonances in thermal and Doppler ducts. *J. Geophys. Res. 94*(D15), 18455–18466.

Gjevik, B. and T. Marthinsen (1978). 3-dimensional lee-wave pattern. *Quart. J. Roy. Meteor. Soc. 104*, 947–957.

Hebert, D., J. N. Moum, C. A. Paulson, D. R. Caldwell, T. K. Chereskin, and M. J. McPhaden (1991). The role of the turbulent stress divergence in the equatorial Pacific zonal momentum balance. *J. Geophys. Res. 96*(C4), 7127–7136.

Ledwell, J. R., E. Montgomery, K. Polzin, L. C. St.Laurent, R. Schmitt, and J. Toole (2000). Evidence for enhanced mixing over rough topography in the abyssal ocean. *Nature 403*, 179–182.

Lighthill, M. J. (1978). *Waves in Fluids.* Cambridge, England: Cambridge University Press.

Lindzen, R. S. and J. W. Barker (1985). Instability and wave over-reflection in stably stratified shear flow. *J. Fluid Mech. 151*, 189–217.

Lipps, F. B. and R. S. Hemler (1982). A scale analysis of deep moist convection and some related numerical calculations. *J. Atmos. Sci. 39*(10), 2192–2210.

McFarlane, N. A. (1987). The effect of orographically excited gravity wave drag on the general circulation of the lower stratosphere and troposphere. *J. Atmos. Sci. 44*, 1775–1800.

Nault, J. T. and B. R. Sutherland (2007). Internal wave transmission in nonuniform flows. *Phys. Fluids 19*, Art. No. 016601.

Ogura, Y. and N. A. Phillips (1962). Scale analysis of deep and shallow convection in the atmosphere. *J. Atmos. Sci. 19*, 173–179.

Palmer, T. N., G. J. Shutts, and R. Swinbank (1986). Alleviation of a systematic westerly bias in general circulation and numerical weather prediction models through an orographic gravity drag parametrization. *Quart. J. Roy. Meteor. Soc. 112*, 1001–1039.

Polzin, K. L., J. M. Toole, J. R. Ledwell, and R. W. Schmitt (1997). Spatial variability of turbulent mixing in the Abyssal Ocean. *Science 276*, 93–96.

Press, W. H., B. P. Flannery, S. A. Teukolsky, and W. T. Vetterling (1993). *Numerical Recipes: The Art of Scientific Computing* (2nd ed.). New York: Cambridge University Press.

Scinocca, J. F. and T. G. Shepherd (1992). Nonlinear wave-activity conservation laws and Hamiltonian structure for the two-dimensional anelastic equations. *J. Atmos. Sci. 49*, 5–27.

Simard, A. and W. R. Peltier (1982). Ship waves in the lee of isolated topography. *J. Atmos. Sci. 39*, 587–609.

Skyllingstad, E. D. and D. W. Denbo (1994). The role of internal gravity waves in the equatorial current system. *J. Phys. Oceanogr. 24*, 2093–2110.

Snively, J. B. and V. P. Pasko (2003). Breaking of thunderstorm-generated gravity waves as a source of short-period ducted waves at mesopause altitudes. *Geophys. Res. Lett. 30*(24), 2254. doi:10.1029/2003GL018436.

Sutherland, B. R. (1996). The dynamic excitation of internal gravity waves in the equatorial oceans. *J. Phys. Oceanogr. 26*, 3214–3235.

Sutherland, B. R. and W. R. Peltier (1992). The stability of stratified jets. *Geophys. Astrophys. Fluid Dyn. 66*, 101–131.

Sutherland, B. R. and K. Yewchuk (2004). Internal wave tunnelling. *J. Fluid Mech. 511*, 125–134.

Walterscheid, R. L., G. Schubert, and D. G. Brinkman (2001). Small-scale gravity waves in the upper mesosphere and lower thermosphere generated by deep tropical convection. *J. Geophys. Res. 106*(D23), 31825–31832.

Wilhelmson, R. and Y. Ogura (1972). Pressure perturbation and numerical modeling of a cloud. *J. Atmos. Sci. 29*(7), 1295–1307.

Yamada, Y., H. Fukunishi, T. Nakamura, and T. Tsuda (2001). Breaking of small-scale gravity waves and transition to turbulence observed in OH airglow. *Geophys. Res. Lett. 28*(11), 2153–2156.

Appendix A

Frobenius Method

A.1 Introduction

In the study of internal wave propagation in shear flows critical layers, which occur at levels z where $\bar{\Omega}(z) = 0$, require special numerical integration techniques. Using typical numerical treatments a critical layer will generate division by zero errors at the singularity introduced by the critical layer. As such, special techniques must be applied to solve both the Boussinesq and anelastic Taylor Goldstein equations near critical layers. To this end, this section develops an approach to avoid integrating across singularities which uses the method of Frobenius.

A.2 The Taylor-Goldstein Equation

For internal waves encountering a critical layer at some height z^*, $\bar{\Omega}(z^*) = 0$. As $\bar{\Omega}$ appears in the denominator of the ϕ coefficient in the Taylor Goldstein equation (2.12) this results in a singularity. The Taylor-Goldstein equation may be rewritten as

$$\bar{\Omega}^2\phi'' + k^2\left(N^2 + \frac{\bar{U}''\bar{\Omega}}{k} - \bar{\Omega}^2\right)\phi = 0, \tag{A.1}$$

which, when certain criteria are met, may be solved near $z = z^*$ using the Frobenius method.

To do this, polynomials must first be fit to the coefficients in equation (A.1). A linear approximation to $\bar{\Omega}$ near the singularity is made at z^*, so that

$$\bar{\Omega}(z) = a(z - z^*), \tag{A.2}$$

and a parabolic fit is made to the ϕ coefficient:

$$k^2N^2 + k\bar{\Omega}\bar{U}'' - k^2\bar{\Omega}^2 = b(z - z^*)^2 + c(z - z^*) + d. \tag{A.3}$$

Using these definitions, equation (A.1) is approximated by the polynomial coefficient fit curves:

$$a^2\hat{z}^2\phi'' + \left(b\hat{z}^2 + c\hat{z} + d\right)\phi = 0, \tag{A.4}$$

where $\hat{z} = z - z^*$. In this form the method of Frobenius may be applied.

The method of Frobenius (see Boyce and DiPrima (2005) section 5.7) assumes that $\phi(z)$ has solutions of the form

$$\phi(z) = \hat{z}^r \sum_{n=0}^{\infty} f_n \hat{z}^n, \tag{A.5}$$

where r and f_n remain to be found. Equation (A.5) is then substituted into equation (A.4) and rearranged into a sum over a single index:

$$\begin{aligned}&\left\{\left(a^2r(r-1) + d\right)f_0 + \left[\left(a^2r(r+1) + d\right)f_1 + cf_0\right]\hat{z}\right\}\hat{z}^r \\ &\quad + \hat{z}^r \sum_{n=2}^{\infty} \left[\left(a^2(n+r)(n+r-1) + d\right)f_n + cf_{n-1} + bf_{n-2}\right]\hat{z}^n = 0.\end{aligned} \tag{A.6}$$

As this equation must hold for all $\hat{z}$ in a region about the singularity, the coefficient for each term in equation (A.6) must equal zero. Considering the $\hat{z}^r$ term, the indicial equation is

$$r^2 - r + \frac{d}{a^2} = 0, \tag{A.7}$$

so that

$$r = \frac{1}{2} \pm \sqrt{\frac{1}{4} - \frac{d}{a^2}}. \tag{A.8}$$

As r must be real to apply the method of Frobenius, it is required that $d/a^2 < 1/4$. This is equivalent to the requirement that the gradient Richardson number is less than $1/4$ at the critical level for wave transmission to occur. Equating the $\hat{z}^{r+1}$ coefficient to zero, f_1 is found in terms of f_0:

$$f_1 = \frac{c}{a^2 r\,(r+1) + d} f_0. \tag{A.9}$$

From the sum in equation (A.6) the remaining coefficients are then recursively defined:

$$f_n = \frac{b f_{n-2} + c f_{n-1}}{a^2\,(n+r)\,(n+r-1) + d}. \tag{A.10}$$

As r and all f_n are now known ϕ may be calculated near the singularity using equation (A.5). In practise, the infinite series is truncated after a finite number of terms, usually on the order of 20 depending on the magnitude of f_n and the width of the region over which the Frobenius solution is required. Using this technique, two solutions are generated, one for each r value. A superposition of these two results is chosen such that the Frobenius solution matches the integrated solution of the regular problem a small step before the critical layer.

A.3 The Anelastic Taylor-Goldstein Equation

To perform the method of Frobenius, the anelastic extension of the Taylor-Goldstein equation (4.17) is first rewritten as:

$$\bar{\Omega}^2 \phi'' + \frac{\bar{\Omega}^2}{H_\rho} \phi' + \left(\frac{k \bar{U}' \bar{\Omega}}{H_\rho} - k^2 \bar{\Omega}^2 + N_\theta^2 k^2 + \bar{U}'' k \bar{\Omega} \right) \phi = 0. \tag{A.11}$$

As in A.2, polynomial approximations are made to the coefficients of the anelastic Taylor-Goldstein equation about a singularity at z^*:

$$\bar{\Omega} = a\,(z - z^*)\,, \tag{A.12a}$$

$$\frac{1}{H_\rho} = b\,(z - z^* - z_1)\,, \tag{A.12b}$$

$$\frac{k\bar{U}'\bar{\Omega}}{H_\rho} - k^2\bar{\Omega}^2 + N_\theta^2 k^2 + \bar{U}''k\bar{\Omega} = c\,(z - z^* - z_2)\,(z - z^* - z_3)\,. \tag{A.12c}$$

The substitution $\hat{z} = z - z^*$ is introduced so that, along with the approximations (A.12), equation (A.11) becomes:

$$a^2\hat{z}^2\phi'' + a^2b\hat{z}^2\,(\hat{z} - z_1)\,\phi' + c\,(\hat{z} - z_2)\,(\hat{z} - z_3)\,\phi = 0. \tag{A.13}$$

To apply the method of Frobenius, ϕ is expanded as in equation (A.5). The ϕ expansion is then substituted into equation (A.11) and rearranged so that like powers of $\hat{z}$ are grouped together:

$$\begin{aligned} 0 = {} & \left[f_0 r\,(r-1)\,a^2 + f_0 z_2 z_3 c\right]\hat{z}^r \\ & + \left[f_1 r\,(r+1)\,a^2 - f_0 r z_1 a^2 b - f_0\,(z_2 + z_3)\,c + f_1 z_2 z_3 c\right]\hat{z}^{r+1} \\ & + \sum_{n=2}^{\infty}\left[f_n\,(n+r)\,(n+r-1)\,a^2 + f_{n-2}c - f_{n-1}\,(z_2+z_3)\,c + f_n z_2 z_3 c\right. \\ & \qquad \left. + \left[f_{n-2}\,(n+r-2) - f_{n-1}\,(n+r-1)\,z_1\right]a^2 b\right]\hat{z}^{r+n}. \end{aligned} \tag{A.14}$$

For this equation to hold independent of $\hat{z}$ the coefficient for each power of $\hat{z}$ must equal zero. Applying this requirement to the $\hat{z}^0$ term and requiring that $f_0 \neq 0$, the indicial equation is obtained:

$$r^2 - r + \frac{z_2 z_3 c}{a^2} = 0, \tag{A.15}$$

this has roots

$$r = \frac{1}{2} \pm \sqrt{\frac{1}{4} - \frac{z_2 z_3 c}{a^2}}. \tag{A.16}$$

As r must be real for the method of Frobenius to be applicable, solutions are possible only when $\frac{cz_2z_3}{a^2} < \frac{1}{4}$. This is again equivalent to the requirement that the gradient Richardson number is less than 1/4 at the critical level for wave transmission to occur. Now that r is known, equation (A.14) is used to relate f_1 to f_0:

$$f_1 = \frac{rz_1a^2b + (z_2 + z_3)\,c}{r\,(r+1)\,a^2 + z_2z_3} f_0. \tag{A.17}$$

And using the sum in equation (A.14), f_n is found recursively in terms of f_{n-1} and f_{n-2} for $n \geq 2$:

$$f_n = \frac{[(n+r-1)\,z_1a^2b + (z_2+z_3)\,c]\,f_{n-1} - [(n+r-2)\,a^2b + c]\,f_{n-2}}{(n+r)\,(n+r-1)\,a^2 + z_2z_3c}. \tag{A.18}$$

Finally, the calculated f_n values are applied to equation (A.5) for each r value and a ϕ solution is generated in a region about the singularity. The two solutions are then superimposed to match the integrated solution as in section A.2.

Appendix B

Thermodynamic Principles

The anelastic numerical solver models internal wave propagation through mean horizontal shear, $\bar{U}(z)$, density scale height, $H_\rho(z)$ as defined by (1.1), and buoyancy frequency, $N_\theta(z)$ as defined by (1.4), profiles. Observed atmospheric profiles are typically prescribed in terms of the background temperature, $\bar{T}(z)$ and pressure, $\bar{\rho}(z)$. Here the tools needed to find H_ρ and N_θ in terms of the background temperature and pressure profiles are developed.

B.1 Thermodynamic Equations

In terms of potential temperature, θ, hydrostatic balance requires

$$\theta \frac{d\pi}{dz} = -\Gamma, \tag{B.1}$$

where Γ is the adiabatic lapse rate, for dry air $\Gamma = 9.571$ K/km. Exner pressure is the absolute pressure scaled by a ground level pressure p_{00}

$$\pi = \left(\frac{p}{p_{00}}\right)^{\kappa}, \tag{B.2}$$

where $\kappa \approx 2/7$ for dry air. Potential temperature is defined as the ratio of absolute temperature to Exner pressure

$$\theta = \frac{T}{\pi}. \tag{B.3}$$

The ideal gas law relates the density to the absolute pressure and temperature

$$p = \rho RT, \tag{B.4}$$

Where $R = 0.287\ \text{kJ/kg} \cdot \text{K}$ is the gas constant.

The absolute pressure distribution is found by integrating the statement of hydrostatic balance presented by equation (B.1) and using equation (B.2):

$$\bar{p}(z) = p_{00}\left(1 - \Gamma \int_{z_0}^{z} \frac{d\xi}{\bar{\theta}(\xi)}\right)^{\frac{1}{\kappa}}. \tag{B.5}$$

Density defined background hydrostatic balance requires

$$\frac{d\bar{p}}{dz} = -g\bar{\rho}, \tag{B.6}$$

where $g = 9.807\ \text{m/s}$ is gravitational acceleration. Applying equation (B.6) to (B.5) the density is found

$$\bar{\rho}(z) = -\frac{p_{00}}{g}\frac{d}{dz}\left(1 - \Gamma \int_{z_0}^{z} \frac{d\xi}{\bar{\theta}(\xi)}\right)^{\frac{1}{\kappa}} = \frac{p_{00}}{R\bar{\theta}(z)}\left(1 - \Gamma \int_{z_0}^{z} \frac{d\xi}{\bar{\theta}(\xi)}\right)^{\frac{1-\kappa}{\kappa}}. \tag{B.7}$$

Applying (1.1) directly to (B.7) the density defined squared buoyancy frequency is found in terms of the potential temperature defined squared buoyancy frequency

$$\frac{g}{H_\rho(z)} = N_\theta^2(z) + \frac{g\Gamma}{\kappa\bar{\theta}(z)}\left(1 - \Gamma \int_{z_0}^{z} \frac{d\xi}{\bar{\theta}(\xi)}\right)^{-1} \tag{B.8}$$

B.2 Numerical Methods

Conversion from the potential temperature to density defined squared buoyancy frequency profile is performed by a two step discrete method. The trapezoid rule is applied to the integrand in equation (B.8) and then H_ρ is found directly:

$$I_n = I_{n-1} + \frac{z_n - z_{n-1}}{2}\left(\frac{1}{\theta_n} + \frac{1}{\theta_{n-1}}\right) \tag{B.9a}$$

$$H_{\rho_n} = g\left[N_{\theta_n}^2 + \frac{g\Gamma}{\kappa\theta_n}(1 - \Gamma I_n)^{-1}\right]^{-1}, \tag{B.9b}$$

where $I_0 = 0$.